NANOMECHANICAL DEPENDENCE OF MICELLES ON SALT LOADING RATIOS: A STORY OF SALT COMPLEXATION, MICELLAR STABILITY, AND NANOPARTICLE SPATIAL DISTRIBUTION

NANOMECHANICAL DEPENDENCE OF MICELLES ON SALT LOADING RATIOS: A STORY OF SALT COMPLEXATION, MICELLAR STABILITY, AND NANOPARTICLE SPATIAL DISTRIBUTION

By Gregory J. Hanta, B. Sc.

A Thesis Submitted to the School of Graduate Studies in Partial Fulfilment of the Requirements for the Degree of Master of Applied Science

McMaster University MASTER OF APPLIED SCIENCE (2019) Hamilton, Ontario
(Engineering Physics)
TITLE: Thesis Example
AUTHOR: Gregory J. Hanta, B.Sc. (University of Guelph)
SUPERVISOR: Dr. Ayse Turak
NUMBER OF PAGES: ix, 98

Abstract

Nanoparticles have been found to have an increasingly wide range of applications including drug delivery systems, chemical sensors, biomolecule sensors, single electron devices, catalysis, Li-ion batteries, and solar cells. A variety of methods have been used to produce nanoparticles, but one widely used approach is the application of reverse micelle nanoreactors whereby block co-polymers are used to encapsulate precursor salts and serve as a vessel for precursor salts to react. As the encapsulation of precursor salts can be a multi-step process, some nanoparticle formulations have proven difficult to make within the reverse micelle nanoreactor. To fully understand the difficulties in nanoparticle formation, we need to have a method to probe the internal structure of the reverse micelle. This thesis presents a novel method for probing the internal structure of the reverse micelle using a quantitative mechanical mapping (QNM) mode for atomic force microscopy (AFM).

Unloaded reverse micelle nanoreactors were analyzed using the QNM AFM mode. A decrease of the Young's modulus was noted through the centroid of the reverse micelle. Many models were applied to describe the noted decrease of Young's modulus. The end result indicated that intrinsic differences between the mechanical properties of polystyrene and poly(2vinyl pyridine) and the co-polymer orientation lead to the measured decrease in Young's modulus through the centroid.

Results from the unloaded case were used to explain changes to the reverse micelle nanoreactor after loading with precursor salts. Across all precursor salts similar trends were noted, however there was no consistent relative Young's modulus or molar salt loading ratio noted within the trends. Three distinct loading zones were consistent across the precursor salts. *Region I* was typified by a slight decrease in relative Young's modulus with small resultant nanoparticles. *Region II* was typified by linear increases in relative Young's modulus for increases in the molar salt loading ratio. *Region III* was found to have two possible outcomes, either the micelle reach a maximum effective infiltration, where the relative Young's modulus ratio no longer increases for increased molar salt loading ratio, or the micelle would unravel for increased molar salt loading ratio. Further studies should be done to confirm the existence of the universal loading regions across further co-polymers, solvents, and precursor salts.

Acknowledgements

I would like to express my deep gratitude to Dr. Turak, my research supervisor, for her patient guidance, enthusiastic encouragement, useful critiques of this research work and advice and assistance in keeping my project on schedule. My grateful thanks are also extended to the rest of the Turak research group for their assistance in acquiring and analysis of the data presented in this research project.

I would also like to extend my thanks to the technicians of the Biointerfaces Institute and the Cranston research group for their help in offering me the resources and equipment needed for this project.

Finally, I wish to thank my parents for their support and encouragement throughout my study.

Contents

List of Figures

Declaration of Academic Achievement

Here, we abuse the abstract command to create the declaration of academic achievement. The page number of this page will need be abused to number correctly.

Chapter 1

Introduction

Recently, nanoparticles have been found to have an increasingly wide range of applications including drug delivery systems, chemical sensors, biomolecule sensors, single electron devices, catalysis, Li-ion batteries, and solar cells.[1, 2] A range of methods have been used to produce nanoparticles, but one widely used approach is the application of reverse micelle nanoreactors whereby block co-polymers are used to encapsulate precursor salts and serve as a vessel for precursor salts to react.[1, 3, 4] The nanoreactor approach is particularly useful as parameters (such as co-polymer block length and solvent) can be tuned to create a nanoparticle array with specific nanoparticle size and dispersion. However, some nanoparticle formulations have proven difficult to make within the reverse micelle nanoreactor.[5] To fully understand the difficulties in nano-particle formation, we need to have a method to probe the internal structure of the reverse micelle. This process is challenging as current in-situ methods are primarily solution based and generally examine small portions of the interactions, failing to provide a whole picture analysis. One approach that seems promising is to use the mechanical properties, An in-depth analysis of the mechanical properties of the reverse micelle could help lead to a better understanding of the loading interactions increasing the efficiency of nanoparticle formation.

In this thesis, to gain a deeper understanding of the mechanisms behind the loading of the reverse micelles, we examined the nanomechanical properties of the unloaded and loaded micelles using a technique known as quantitative nanomechanical mapping atomic force microscopy (QNM-AFM). We analyzed a variety of co-polymers used to make reverse micelles, different dispersion conditions such as solvents, different

salts, and loading ratios to try to determine a correlation between the nanomechanical properties and the resultant nanoparticle arrays.

Chapter 4 explores the properties of the unloaded reverse micelles. The QNM-AFM results here showed a decrease in the Young's modulus of the reverse micelle through the centroid centre of the micelle. This decrease was consistent for all three co-polymers used. Three possible models were compared to describe the decrease in Young's modulus across the centroid. The results indicated a combination of an intrinsic difference and polymer brush model best described the observed changes in nanomechanical properties across the micelle.

Chapter 5 explores the loading of the reverse micelle with iron chloride. The QNM-AFM results indicate a relationship between the relative Young's modulus changes, the molar ratio of additional salt, and the final nanoparticle size. This leads to a prediction on the dispersion and stability of a particular molar loading ratio. For the iron chloride, the complexation of the iron chloride with the P2VP drive the features shown.

Chapter 6 expands the QNM approach to examine the effect of solvents on the unloaded micelles and the loading of precursors. Solvents are a key approach to affecting the size and dispersion of nanoparticles. Again QNM derived Young's modulus for the micelles was correlated to the resultant nanoparticle distributions. This suggests a universality of the QNM approach for reverse micelle deposited nanoparticles.

This is explored in detail in Chapter 7, where we examined the loading of reverse micelles with indium acetate, zinc acetate, tin chloride, and methylammonium iodide. Our interest was to establish if the maximum relative Young's modulus, molar loading ratios and the trends observed would be generally applicable. Though the absolute values of the loading ratios and relative Young's modulus were not consistent, our results showed the trend to be the key universal factor of these study, with three regions describing the full behaviour of micelles as a function of various parameters.

Chapter 8 describes the key conclusions from this thesis with Chapter 9 suggesting further extensions to verify and extend the universality described above.

Chapter 2

Literature Motivation

2.1 Reverse Micelle Synthesis

Di-block co-polymers can provide a cost-effective bottom-up synthetic route for fabricating nanoparticle arrays with high tunability and controllability in terms of size, shape, and spacing.[6–8] This is the result of their two chemically different blocks which leads to the formation of core-corona micelles or reverse micelles in selective solvents. Reverse micelle nanoreactors are advantageous as it can create nanoparticle arrays with exact sizing and spacing by tunning the polymer block length and the solvent used. Reverse micelles become a powerful method to synthesize nanoparticle arrays of metals, metals oxides, and metal alloys through the incorporation and loading of the proper metal precursors, which usually possess higher affinity to the hydrophilic block.[1, 8, 9] The interaction mechanisms between loading salts and the diblock co-polymer will be explored in **Section 2.1.2**.

A key strength of the reverse micelle nanoreactor process is the wide variety if tunable parameters than can affect the nanoparticles. These parameters include, but are not limited to, the type of di-block co-polymer, the molecular weight of the di-block co-polymer, solvent, loading ratio, and stirring time. Modifications of these parameters in the loading process have been shown to result in changes to the size resultant nanoparticles and spacing of the resultant nanoparticle array. They can also affect the morphology and spacing of the micelles themselves.

Figure 2.1 give a schematic representation of the reverse micelle nanoreactor process for nanoparticle formation. Di-block co-polymers are dissolved in a non-polar
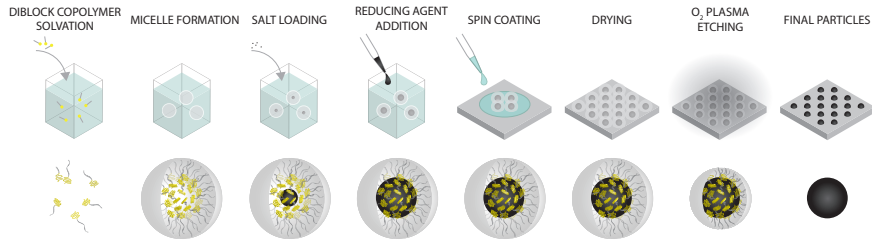
Figure 2.1: A schematic representation of the reverse micelle nanoreactor process for nanoparticles. Di-block co-polymers are first dissolved in a non-polar solvent, which create reverse micelles. The reverse micelles are then loaded with precursor salts (and occasionally reducing agents) to create the nanoparticle. The solution is then spin coated on a substrate to create an array of loaded micelles. The micelles are etched away using oxygen plasma to reveal to nanoparticle array.

solvent to create a solution of reverse micelles. Precursor salts are added to the reverse micelle solution and are incorporated into the centre of the micelle through osmosis or by direct interaction with the polymer block located in the core of the micelle. Occasionally, reducing agents are added after the precursor salt to cause the nanoparticle to completely form within the core of the reverse micelle. The looaded reverse micelles are spin coated onto a substrate to create an array of micelles. Finally, the di-block co-polymer is etched away using oxygen plasma to reveal the nanoparticle array.

2.1.1 Effect of Polymer Morphology on Nanoparticle Synthesis

The size and spacing of the nanoparticles is often linked back to the reverse micelle size, in particular the total micelle diameter and micelle core diameter have been known to affect the resultant nanoparticle size and array order. Multiple studies have analyzed the effect block length (and by extension molecular weight (M_N)) will have on the resulting morphology of co-polymer solutions.[10, 11] Results from such studies show that the morphology of a co-polymer solution can be altered by changing the block lengths of the co-polymer. Morphologies can range from spherical micelles, to rod-like micelles, to vesicle micelles. The studies in questions indicate that decreasing the block length of the corona co-polymer block while holding the core co-polymer block constant will lead to the creation of micelles with a larger core diameter.[10] The larger core diameter is generally thought to lead to larger resultant nanoparticles.

The block lengths of the co-polymers used can also lead to changes in the sizing and spacing of nanoparticles created using the reverse micelle nanoreactor method. For instance, Moffitt et al[12, 13] generated size control cadmium sulfide(CdS) nanoparticles via polystyrene-*block*-poly(acrylic acid) (PS-*b*-PAA) with different PS and PAA block length. Using polystyrene-*block*-poly(2vinyl pyridine) (PS-*b*-P2VP), Spatz et al[14] tailored the size and spacing of the resultant gold(Au) nanoparticles by varying the lengths of P2VP and PS block. Additional examples indicate that the size of the nanoparticle is determined by the amount of metal salt that can be incorporated into the micellar core indicating that the nanoparticle size can be determined by the length of the core block.[15]

In addition to the molecular weight and block length, solvents have also been studied as a way to tune the morphology of polymer films. Polymer size and concentration, film deposition rate, and solvent type have all been linked to the final morphology of a deposited polymer films.[16, 17] Theoretically, the degree of polymerization of a co-polymer can lead to the expression of varying morphologies and can also effect the corona thickness to core radius ratio.[17] Varying morphologies have also been noted experimentally as a function of dip coating rate and solvent.[16] Here, it was noted that different solvents will produce larger micelles but at different dip coating rates.[16] The exhibition of various morphologies for block co-polymers has further been explored as a function of the percent weight of solvent used.[18]

The production of various morphologies seems to be linked to the properties of the solvents used. Studies have indicated that solvents can have varying swelling parameters, cross-links densities, and Flory-Huggins parameters.[19–21] The cited parameters have been linked to the volume and size of polymer films but have not been extensively used to study the mechanical properties.

Though solvents have been widely cited as a way to tune the morphology of polymer films, limited research has been done on how solvents effect the mechanical properties of polymer films and micelles. In the case of micelles, it has been hypothesized that variations in solvents could lead to an increase in interfacial energy between the solvent and the core block, increasing the stretching of the core block and leading to larger micelles.[10]

2.1.2 Effect of Loading Interactions on Nanoparticle Synthesis

Typically, nanoparticles are formed in the reverse micelle through the incorporation of precursors salts within the hydrophilic block due to their higher affinity to the hydrophilic block. A relationship between the size of the nanoparticles and the amount of metal precursors loaded with fixed block length for di-block co-polymers of PS-*b*-PAA[22],PS-*b*-P2VP[15, 23], polystyrene-*block*-poly(ethylene oxide) (PS-*b*-PEO)[24] and polystyrene-*block*-poly(4vinyl pyridine) (PS-*b*-P4VP)[25]. The size of resultant nanoparticles depends on the amount of precursors that can be infiltrated into the micellar core.

However, previous studies have indicated variable success in producing nanoparticles of a specfic composition from reverse micelles. The formation of indium tin oxide with a 6% doping of tin was possible in solution, but proved impossible in the reverse micelles.[5] When similiar precursor reactants were used in the reverse micelle, the net result was an extremely lowly indium doped tin oxide.[5] It was hypothesized that this failure to create nanoparticles of a similar formulation in the reverse micelles was due to the different interactions between the hydrophilic block and the different precursor salts resulting in limited infiltration.

Though previous studies have provided a link between loaded percursor salt and the size of the nanoparticle, they do not intensely explore the infiltration mechanism nor a maximum limit of infiltration for the precursor salt. Studies which provided a link between the loaded percursor salt and the size of the nanoparticle primarily analyzed the solution after deposition on a substrate.[22–25] Post-deposition analysis used imaging techniques such as TEM, SEM, AFM to confirm changes to the nanoparticle and micellar sizes and UV-vis and XPS to confirm the molecular composition of the nanoparticles. A handful of studies performed measurements of the loaded micelles in-situ, employing techniques such as DLS to confirm changes in the size of the micelle and FTIR to confirm changes to the molecular composition.[5, 22] Though analysis has confirmed the presence of the precursor salt in the reverse micelle, little work has been done to quantify how much of the precursor salt is incorporated and what changes precursor salt loading has on the reverse micelle system.

Recently, Hans-Gerd Boyen's group[26] found that the loading of $NbCl_5$ and $FeCl_3$ into PS-*b*-P2VP reverse micelles resulted in poor size distribution and dispersion of

the resulted NPs above certain loading ratio. Up to 1.0 loading ratio of the $HAuCl_4$ was suggested to be the maximum loading of the PS-*b*-P2VP reverse micelles.[14] Sageshima[27] reported that the Fe^{3+} ions hybridized with P2VP blocks mainly through intramolecular coordination, indicating the existence of the saturation loading of $FeCl_3$.

Additional studies have shown that most precursors have some interaction with the P2VP block of our reverse micelle system. The mechanism of infiltration has been explored and can be linked with the amount of the precursor loading and the order of the resultant nanoparticle array due to the complex coordination and binding interaction between the micellar core and the inorganic precursor. Therefore, finding a way to predict the threshold precursor loading of the micelles could be helpful for developing precursor-micelles interaction mechanisms and improving the size controllability of the resultant nanoparticles.

2.2   Measuring Nanomechanical Properties

Many methods have been explored to analyze the mechanical properties of soft films using multiple measures. Numerous nanoparticle formulations that employ the reverse micelle technique rely on a multi-step infiltration yet, there are very few methods available to confirm the infiltration of the precursor salts to the micelle core. Studies have shown that the infiltration of precursor salts will modify the nanomechanical properties of the reverse micelles.[28, 29] Yet no systematic analysis of this effect has been studied.

2.2.1   Nanoindentation

Nanoindentation is one of the more common methods used to accurately and repeatedly measure the elastic modulus of polymer films.[30–32] However, nanoindentation relies on indentation depths on the order of the hundreds of nanometers to accurately measure the elastic modulus of the sample.[30–32] For the reverse micelle nanoreactor process, monolayer films of micelles with an estimated thickness of less than 50 nm are typically used. As such, nanoindentation is not a suitable technique to confirm the change in elastic modulus due to the large size in indentation depth relative to the thickness of our micelle film. Further, typical nanoindentation techniques rely on mechanical or optical analysis of the contact area after indentation.[30, 33] The

7
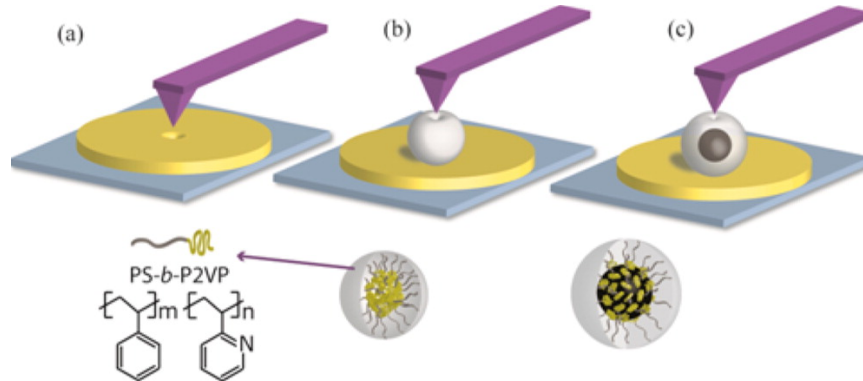
Figure 2.2: A schematic representation of the tapping mode atomic force microscopy (TM-AFM) nanindentation method used by Solmaz *et al.* The substrate (A), unloaded micelle (b), and loaded micelles (c) were all probed at approximately the centre of the micelle with an AFM tip to compare the force indentation curves.[28]

vast majority of polymers are quite soft, as such, minimal deformation is seen after indentation, leading to unreliable elastic modulus measurements.[30, 33]

The reverse micelle nanoreactor has been studied with a nanindentation technique through the use of tapping mode atomic force microscopy (TM-AFM). TM-AFM can be used to directly measure the elastic modulus of a sample by nanoindentation measurements.[28] TM-AFM nanoindentation differs from typical nanoindentation methods, as the indentation depths used are less than 10 nm.[28] TM-AFM has been used to confirm the loading of precursors into reverse micelles.[28, 29] Solmaz *et al.* used a TM-AFM and force indentation curves to analyze the elastic modulus of loaded reverse micelles.[28] **Figure 2.2** shows a schematic represtantion of how Solmaz *et al* acquired the force indentation curves. Measurement were taken aboive the centre of the micelle. They calculated the elastic modulus by indenting the AFM cantilever tip at the approximate centre of the reverse micelle to generate a force-indentation curve.[28] The sample's elastic modulus was extracted by applying a Hertz model to the loading region of the curve. However, it may not be capable of indicating the amount of precursor infiltration as it is challenging to verify that indentation measurements are taken above the centre of the loaded micelle core.[28]

2.2.2   Tapping Mode Atomic Force Microscopy

Atomic force microscopy (AFM) has proven to be a useful tool for measuring the nanomechanical properties of films through the use of the force-distance curves they

can produce.[34] Studies have demonstrated that changes in di-block co-polymer film composition can be measured using tapping-mode AFM (TM-AFM).[28, 29, 35] TM-AFM combines the topography and phases images to create a contour plot which shows the variation in mechanical properties as a result of changes to the composition of the film.[29, 35] Aytun *et al.* saw increased phase contrast but could not quantify the degree of the phase changes.

2.2.3   AFM QNM

Quantitative nanomechanical (QNM) mapping modes for AFM is a new technique that has been developed, allowing users to map the topography and modulus of a sample simultaneously.[31, 32, 36] QNM modes work by fitting a model to the force-indentation curve generated by the AFM, allowing for the instantaneous mapping of mechanical properties.[31, 32, 34, 36, 37] In essence, the QNM technique combines the nanoindentation and AFM phase mapping techniques.

Studies have shown that QNM AFM modes can reliably measure elastic modulus values for a variety of polymer films similar to those measured by more common nanoindentation techniques.[31, 32] This method is primarily used for organic systems and has not be widely applied and adapted to materials science. QNM shows the most potential of the methods explored as QNM can reliably quantify changes in the reverse micelles films. In this thesis we apply a QNM model to the reverse micelle nanoreactor system. We use the Derjaguin-Müller-Toporov (DMT) model to quantify changes to the reverse micelle nanoreactor following the loading with precursor salts.

Figure 2.3 shows an example of how the QNM mode can be applied to reverse micelles. Unloaded films (**Fig. 2.3 (a)** can be prepared and a Young's modulus map generated for the surface (**Fig. 2.3 (b)**, allowing the user to examine the profile of the Young's modulus through a reverse micelle (**Fig. 2.3 (c)**. The some procedure can be followed for a film of loaded micelles (**Fig. 2.3 (d)**, allowing the user to compare the behaviour of the Young's modulus through a loaded micelle to that of the unloaded case.
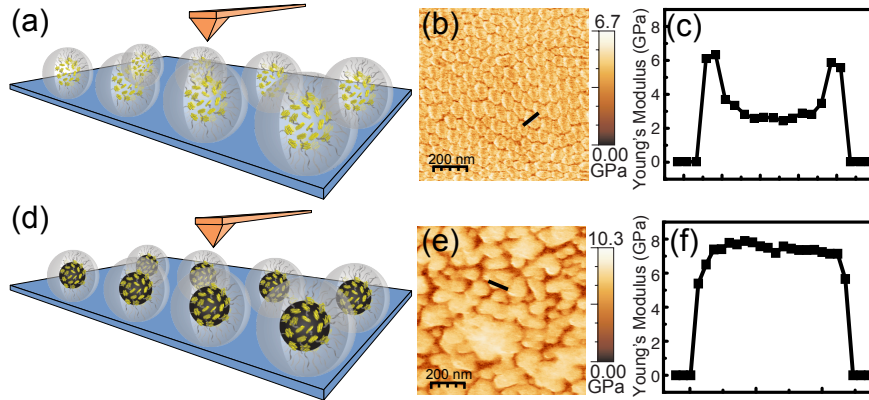
Figure 2.3: A schematic representation of the application on the quantitiative nanome-hcanical (QNM) mode for AFM. Unloaded micelles are arranged on the surface of a substrate (a). A Young's modulus map is produced (b) instantaneously for every point using the DMT model, allowing for users to examine the behaviour of the Young's modulus through a single reverse micelle (c). The same procedure can be followed for a film of loaded micelles (d), where a Young's modulus map (e) and a profile of the Young's modulus (f) can be created and compared to the unloaded micelle. This figured will be explained in detail in **Chapter 5**.

2.3   QNM Theory

In order to instantaneously map the mechanical properties of a film, the interaction of the AFM probe tip with the micelle film must be quantified through the generation of a force-indentation curve. The mehcanical properties of each interaction point can be calculated using the Derjaguin-Müller-Toporov (DMT) model. The reduced elastic modulus is obtained at each interaction point by fitting the DMT model to the unloading portion of the force-indentation curve (i.e. where the AFM tip is retracting from the surface) (Eq. (4.1)).[31, 38]

$$F_{tip} = \frac{4}{3}E^*\sqrt{Rd^3} + F_{adh} \tag{2.1}$$

Where E^* is the reduced elastic modulus, F_{tip} is the force on the AFM tip, F_{adh} is the adhesion force between the AFM tip and the sample (the lowest point on the retract curve), R is the radius of the AFM tip, and d is deformation depth.[31, 38]

The reduced elastic modulus (E^*) can be related to the sample elastic modulus (E_s) by

$$E^* = \frac{(1 - \nu_t^2)}{E_t} + \frac{(1 - \nu_s^2)}{E_s} \qquad (2.2)$$

In Eq. (4.2), E_t is the elastic modulus of the AFM tip, ν_t is the Poisson's ratio of the AFM tip, and ν_s is the Poisson's ratio of the sample.[31, 38] As the AFM tip is much stiffer than the sample, we assume E_t to be infinite, causing the first term of the equation to become negligible.[31] The resulting modulus maps present the sample elastic modulus (E_s).

The DMT model is used in this thesis to create Young's modulus maps of the loaded and unloaded polymer films and was able to quantify the changes in the reverse micelle system.

Chapter 3

Experimental Methods

3.1 Nanoparticle Synthesis

As discussed in **Chapter 2.1**, nanoparticles were created using the reverse micelle nanoreactor method. Our method involved the dissolving of polystyrene-*block*-poly(2vinyl pyridine) (PS-*b*-P2VP) co-polymers of various block lengths in non-polar solvents. Once the co-polymer was dissolved, precursor salts would be added to the solution to load the reverse micelles.

3.1.1 Polymer Fritting

Prior to dissolving in non-polar solvents, the di-block co-polymer PS-*b*-P2VP was fritted to remove undesirable oxidation. Twice the volume of tetrahydrofuran(THF) relative to a polymer was added in a polymer(PS-*b*-P2VP) containing vial. The vial was sonicated for 30 minutes until all the polymer was dissolved. The solution (polymer dissolved in THF) was filtered using glass fiber and precipitated into 200L of hexane stirred at 500rpm. The hexane solution was vacuum filtered using a "fine" pore size filter funnel(**Fig 3.1**(b)). The filtered precipitation was dried overnight in the ambient environment. The dried powder was used to form the reverse micelles.
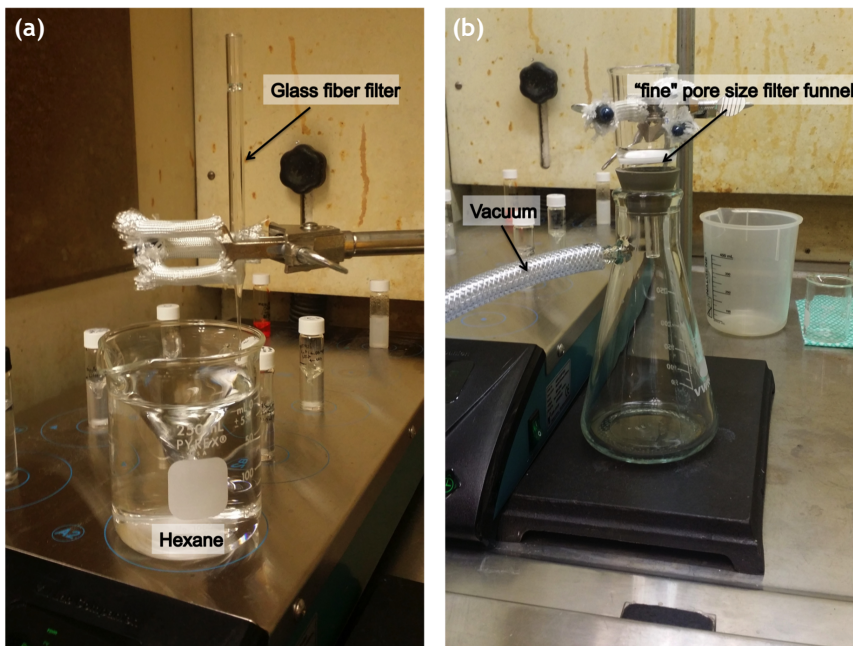
Figure 3.1:   A picture showing the experimental set up for the fritting of the diblock co-polymer. The polymer-THF solution is run through a glass wool filter and precipitated in hexane (a) before being vacuum filtered through a fine filter (b).

3.1.2   Reverse Micelle Formation

10 mL vials were cleaned in sequential ultrasonic baths of 30 minutes each of acetone and ethanol. After cleaning with solvents, the vial was dried with N_2. To achieve reverse micelles formation above the critical micelles concentration (3 gL^{-1}), 15 mg of PS-b-P2VP was dissolved in 5 mL of toluene and stirred for 24 hours. The size of reverse micelles in solution were determined by dynamic light scattering using Zetasizer Nano (Malvern) and confirmed by atomic force microscopy (Nano Scope IIIa, Veeco) after dynamic spin coating onto silicon substrates, as described in **Chapter 3.2** and **Chapter 3.3**.

3.1.3   Precursor Salt Loading

In order to form nanoparticles, precursor salts were added sequentially to the micelle solution and kept under magnetic stirring at 1,500 rpm for 2 days for each salt. In between each addition of reagent, the solutions were decanted into Eppendorf tubes and centrifuged for 8 minutes at 15,000 rpm to remove unloaded salts. The supernatant

solution from the tubes were pipetted back into the original vial, which had been rinsed with toluene. The typical sequence followed was dependent on the desired final nanoparticle, but typically followed the addition of precursor salt (e.g. tin chloride, iron chloride, lithium hydroxide, etc.) which was allowed to spin for 2 days before the addition of a reducing agents (e.g. ethanol, hydrogen fluoride, etc.) which was also allowed to spin for two days days stirring), Sn salts (2 days stirring) before post processing as described in **Chapter 3.2**.

3.2 Post Processing

3.2.1 Coating on Substrate

In all cases, solution were deposited on a silicon substrate. Prior to use, all substrates were cleaned in an ultrasonic bath of 30 minutes each of acetone and ethanol sequentially. After cleaning with solvents, all substrates were dried with N_2. The solutions were then coated on to the substrates using spin coating. For spin coating, $3\mu L$-$5\mu L$ of micellar solution was dynamically spin coated on substrates for 45 seconds, using a Laurell Technologies Spin coater(WS-650MZ-23NPP). The spin coating rate was varied from 2,000 to 6,000 rpm.

3.2.2 Plasma Etching

The specimens were plasma treated under oxygen to remove the polymeric micelles and leave nanoparticles on the substrates with Harrick Plasma cleaner (PDC-001-HP). Etching condition was set as 29.6 W power, 5 mbar O_2 gas pressure, and 30 sccm O_2 gas flow rate for 25 minutes.

3.3 Analysis Techniques

3.3.1 Atomic Force Microscopy

Atomic force microscopy (AFM) images were collected by an Asylum MFP-3D instrument(Oxford Instruments Asylum Research Inc.) in the alternating current mode under ambient environment. AFM probes(Oxford Instruments Asylum Research Inc.)with

springconstant of 26 N/m and resonant frequency at 300 kHz were applied in tapping mode for topography scan. WSxM was used to process the AFM raw data.

3.3.2   Quantitative Nanomechanical AFM

Quantitative nanomechanical (QNM) AFM was done using a Bruker Bioscope Catalyst with an RTESPA probe. The probe was selected to match the range of elastic modulus we were investigating based on recommendations by Bruker. For each round of measurements, the probe was calibrated using a relative method of calibration, using a sample of known modulus. The calibration first involves the calculation of the deflection sensitivity by ramping the probe into a clean sapphire substrate provided by Bruker. A minimum of three ramps were done and the average deflection sensitivity was used. The probe is then withdrawn from the substrate and a thermal tune is preformed to calculate the spring constant. Lastly, a polystyrene sample of known modulus provided by Bruker is loaded and imaged. The tip radius is adjusted until the measured modulus agrees with the known modulus. AFM images were taken on a scale of 1 μm x 1 μm and at a scanning rate of 0.5 Hz.

AFM images were analyzed in post using WSxM. The elastic modulus was determined by taking a line profile through 100 micelles by matching the coordinates in the topography channel to the elastic modulus channel. The resulting line profiles showed a variable elastic modulus through the centre of the micelle. Due to the variability, the elastic modulus for each micelle was determined by taking the average of the centre points of the line profile. The number of points averaged to determine the modulus varied due to a range in the size of micelles measured. However, typically 10 points were taken. The modulus measurements for each micelle were fit using a Gaussian approximation to calculate the average modulus value and error for each treatment.

3.3.3   Scanning Electron Microscopy

The substrates for scanning electron microscopy(SEM) characterization were P-doped silicon wafers which were conductive enough to allow the direct SEM imaging of micelles or nanoparticles without coating. The micelle or nanoparticle coated substrates were mounted by carbon tape and nickel paste on 25.4 mm standard aluminium stubs. The SEM characterizations were conducted in FEI Versa 3D SEM with a Schottky thermal

field emitter electron gun. The accelerating voltage and probe current were normally adjusted to 5kV and 12 pA to minimize the charging effect, which still maintained good signal-to-noise ratio for high-quality imaging.

3.3.4   Dynamic Light Scattering

Zetasizer Nano, Malvern Instruments Ltd. was used for dynamic light scattering (DLS) measurement. A quartz cuvette should be used because quartz cells endure a toluene solution. The detector used Non-Invasive Backscattering(NIBS) optics with scattering angle 173°, and a He-Ne laser (4.0 mW) used as a light source with wavelength 633 nm. Reference values for polystyrene (refractive index = 1.59) which makes up the corona of micelle was used for the optical parameter, and the micelles solution(0.54 cP) value used to account for the viscosity value of dispersion.

Chapter 4

Empty Micelle Modelling

4.1 Introduction

The use of reverse micelles as nanoreactors for the formation of nanoparticles is a widely used technique. In order develop a comprehensive model of the interactions surrounding the loading of the reverse micelles, we first had to gain a deeper understanding of the Young's modulus through the reverse micelle. We had noticed unusual trends in the unloaded micelle map and preformed a full investigation to determine the underlying reason for these trends. As discussed in chapter 2, the reverse micelle nanoreactors employed by our process are formed from a polstyrene poly-2-vinylprydiene co-polymer.

4.2 Experimental Methods

In this study, we used three polystyrene-*block*-poly(2vinyl pyridine) (PS-*b*-P2VP) co-polymers. All three co-polymers underwent a cleaning process before being used. The PS-*b*-P2VP was dissolved in THF and filtered using a glass wool filter to remove any large debris. The filtered solution was precipitated out in hexane and pumped through a filter to remove the polymer precipitate from the hexane, leaving a fine, uniform co-polymer powder.

Polymer solutions were prepared by dissolving 15 mg of the fritted co-polymer powder in 5 mL of a non-polar solvent, in this case toluene. The co-polymer and toluene solution were allowed to spin on a stir plate at room temperature for 24 hours to form reverse micelles.

Mono-layer co-polymer films were prepared for quantitative nanomechanical mapping (QNM) by spin coating 4 µL of the co-polymer toluene solution on a clean silicon substrate. The mono-layer films were analyzed by atomic force microscopy (AFM) using the QNM mapping mode described in Section 4.3. Both topography and Young's modulus maps were collected for each sample and line profiles were used to determine the trend of the Young's modulus across the micelle. Sample maps and line profiles of this process can be seen in **Figure 4.1**.

Due to the variability, the elastic modulus for each micelle was determined by taking the average of the centre points of the line profile. The number of points averaged to determine the modulus varied due to a range in the size of micelles measured. However, typically 10 points were taken. To calculate the Young's modulus for the whole sample, 100 individual micelles were measured using the above technique and fit using a Gaussian approximation. Errors on the Young's modulus were taken as the half-width half-max value of the Gaussian approximation.

In addition to the Young's modulus, we also prepared samples of the empty micelle polymers for transmission electron microscopy (TEM) to calculate the core diameter and scanning electron microscopy (SEM) to calculate the the micelle diameter. Sample preparation for TEM required an iodine staining process. Iodine can be used to enhance contrast in electron microscopy of diblock co-polymers as iodine will preferentially stain pyridine over polystyrene.[39, 40] Empty micelles are typically displayed in SEM/TEM with very low contrast as a result of the weak elastic interactions of carbon and nitrogen with energetic electrons, without a significant difference for PS and P2VP blocks. By exposing the empty micelles to an iodine vapour, the P2VP cores can be made visible due to the preferential complexation of iodine and pyridine, with a binding energy of 0.39 eV.[41]

To prepare the stained samples, a thin layer of micelles was deposited on the porous carbon thin film TEM grids using a dip-coating approach, allowing for direct TEM characterization of the individual micelles. To selectively stain the P2VP cores, the micelles coated TEM grids were exposed to I_2 vapour for 3 hours at room temperature, by placing iodine crystals and the TEM grids in a sealed glass container.[42–44] TEM was preformed at 200 kV to determine the diameter of the P2VP micellar cores.

Both the TEM and SEM images were analyzed using ImageJ. Micelle diameters were extracted from the images. The major and minor diameter for each micelle were averaged and 100 micelles were selected at random to determine the average
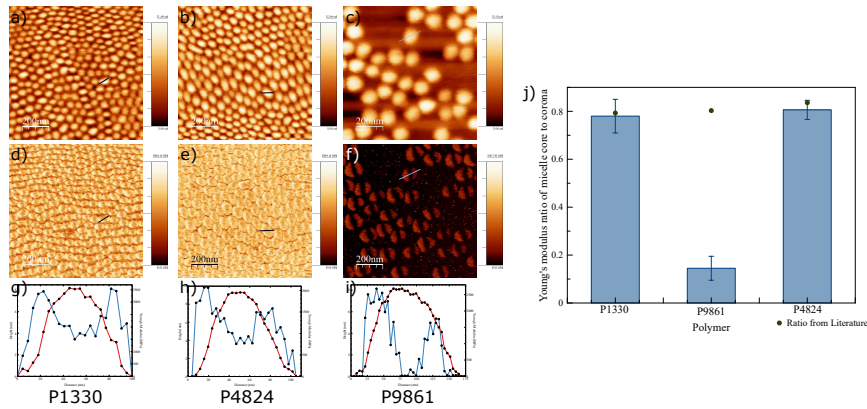
Figure 4.1: All three micelles types were analyzed using a QNM mode for AFM. The topography channel [a), b), c)] were combined with the Young's modulus channel [d), e), f)] to see how the modulus changes across the same micelle using line profiles [g), h), i)]. A comparison of the line profiles shows that each micelle experiences a decrease through the centroid. The ratio between the Young's modulus for the core and corona is within error of the expected literature value for P1330 and P4824 but very far off for P9861 [j)].

diameter for the co-polymer using a Gaussian approximation. The corona thickness was calculated by subtracting the micellar diameter from the corona diameter and dividing by two. An example of SEM and TEM images used can be seen in **Figure 4.2**

4.3   Young's Modulus Mapping

Before we can confirm the infiltration of precursor salts to the core of the reverse micelle nanoreactors, we had to first develop a better understand of the mechanical properties of the empty micelles nanoreactors. We were able to examine the mechanical properties of the micelles through the creation of Young's modulus maps using a quantitative nanomechanical mapping (QNM) mode of an atomic force microscope (AFM). The QNM mode was provided by the Bruker Nanoscope software. The Young's modulus maps were created by quantifying the interaction of the AFM probe tip with the micelle film through the generation of a force-indentation curve. The elastic modulus of each interaction point was calculated using the Derjaguin-Müller-Toporov (DMT) model. The reduced elastic modulus is obtained at each interaction point by fitting the DMT model to the unloading portion of the force-indentation curve (i.e. where

the AFM tip is retracting from the surface) (Eq. (4.1)).[31, 38]

$$F_{tip} = \frac{4}{3}E^*\sqrt{Rd^3} + F_{adh} \tag{4.1}$$

Where E^* is the reduced elastic modulus, F_{tip} is the force on the AFM tip, F_{adh} is the adhesion force between the AFM tip and the sample (the lowest point on the retract curve), R is the radius of the AFM tip, and d is deformation depth.[31, 38]

The reduced elastic modulus (E^*) can be related to the sample elastic modulus (E_s) by

$$E^* = \frac{(1 - \nu_t^2)}{E_t} + \frac{(1 - \nu_s^2)}{E_s} \tag{4.2}$$

In Eq. (4.2), E_t is the elastic modulus of the AFM tip, ν_t is the Poisson's ratio of the AFM tip, and ν_s is the Poisson's ratio of the sample.[31, 38] As the AFM tip is much stiffer than the sample, we assume E_t to be infinite, causing the first term of the equation to become negligible.[31] The resulting modulus maps present the sample elastic modulus (E_s).

4.4   Results

As seen in the smaller graphs of **Figure 4.1**, all three co-polymers used show variability of the elastic modulus through the empty micelle. In all cases, we saw that the elastic modulus for the micelle is stiffer on the edges and lower through the core. The exact values for the Young's modulus at the edge and core of each micelle are noted in **Table 4.1**, which shows that the value for Young's modulus is dependent on the co-polymer.

Table 4.1 indicates that P1330 has a larger modulus than P4824. A possible mechanism for this could be the relationship between the average molecular weight (M_N) and core radius.[10, 11] To examine this, we used SEM to determine the average micelle diameter and iodine staining with TEM to determine the core diameter. While both P4824 and P1330 have a similar core (P2VP) block length, P1330 has a much lower corona (PS) block length and P4824. The lower block length leads to an increased core diameter and corona thickness in P1330. The increased chain stretching in the corona of P1330 could be the reason P1330 exhibits a larger Young's modulus than P4824, as it has been indicated that the stretching of polymer molecules leads to a major increase in the Young's modulus of the polymer.[45]
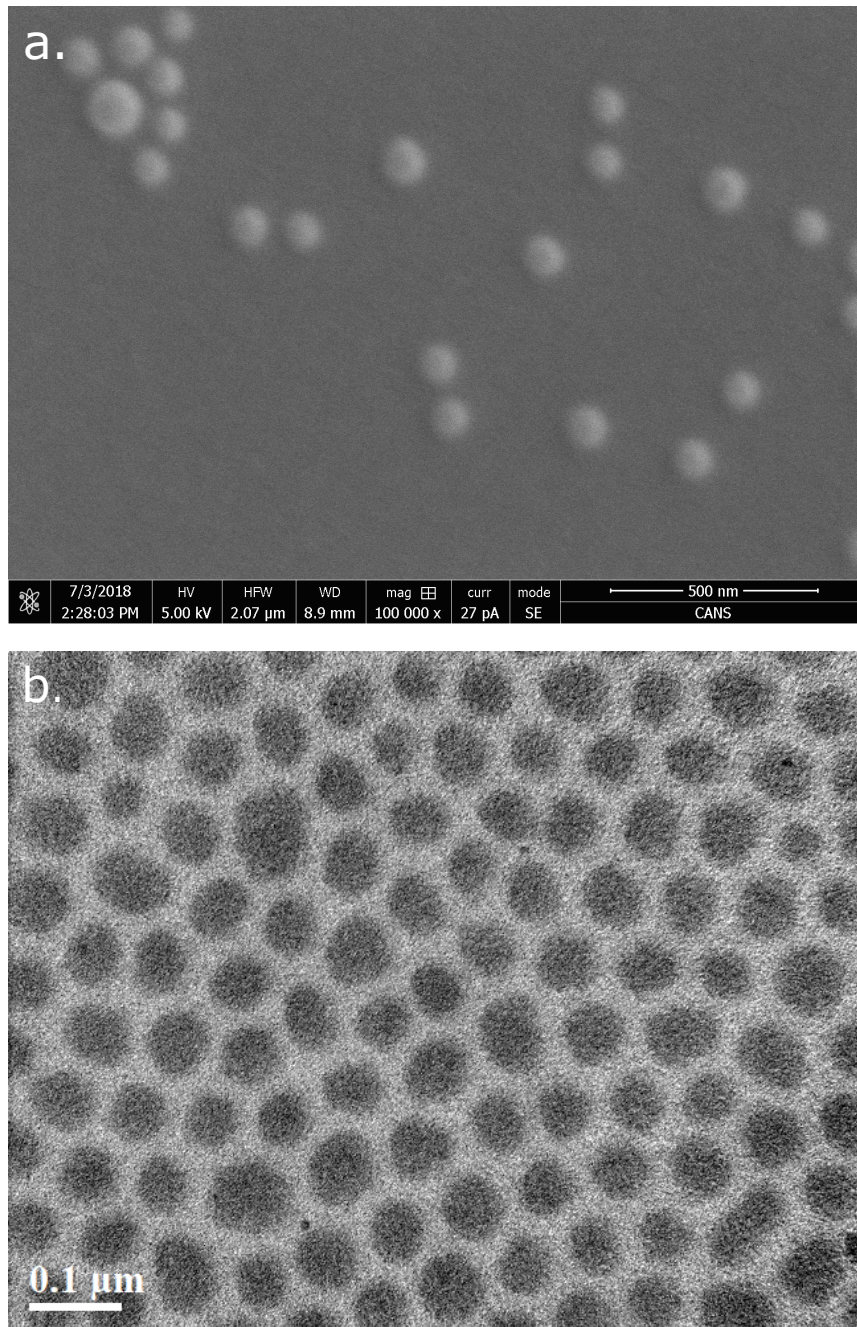
Figure 4.2: SEM (a) and TEM (b) images of the P9861 micelles. SEM images were used to determine the whole micelle diameter while TEM images were used to determine the micelle core diameter.

Table 4.1: Properties of the co-polymers used as reverse micelle nanoreactors during experiements

	1330	4824	9861
P2VP:PS	1.44	0.89	1.28
P2VP M_N (x 10^3)	70	66.5	36
PS M_N (x 10^3)	48.5	75	28
Micellar Diameter (nm)	56.26 ± 3.90	41.12 ± 3.64	94.57 ± 4.01
Core Diameter (nm)	40.88 ± 3.26	30.86 ± 4.10	74.66 ± 3.92
Corona Thickness (nm)	7.69 ± 2.54	5.13 ± 2.74	9.96 ± 2.80
Micelle Core Young's Modulus (GPa)	2.51 ± 0.06	2.24 ± 0.05	0.17 ± 0.07
Micelle Edge Young's Modulus (GPa)	3.22 ± 0.11	2.78 ± 0.13	1.17 ± 0.12

However, this mechanism does not explain the trend of Young's modulus across the micelle (harder on the edge and softer through the middle) and further fails apart when applied to the P9861. As P9861 has even smaller molecular weights than P1330, it is expected to produce a smaller micelle.[11] As evident from **Table 4.1**, that is not the case the P9861 produces a large micelle.

The large micelle diameter for P9861 noted in **Table 4.1** was calculated from a SEM image similar to **Figure 4.2 a)**. When we compare the SEM results to the AFM images seen in **Figure 4.1 c) and f)**, we see a similar radius. However, the micelle height noted in **Figure 4.1 i)** shows a micelle height of 8 nm. The small height of 8 nm is accompanied with an extreme decrease in Young's modulus, seemingly indicating that the micelle has collapsed when it was deposited on the sample. We believe these micelles balloon in solution but collapse when they are deposited on a sample.

Based on the large micelle diameter, extreme decrease of Young's modulus and perceived in-solution ballooning on the P9861 micelle we believe the P9861 to be producing a crew-cut micelle, as per **Figure 4.3**. A crew-cut micelle is a micelle with a large core diameter and relatively thin corona,[6, 46] We can see in **Table 4.1** that P9861 has the smallest corona thickness relative to core diameter, separating it from the other two polymers, further confirming our hypothesis.

We can conclude that we will need a more robust mechanism to describe why the Young's modulus is stiffer on the edge of the micelle and lower through the core. Three more robust mechanisms were examined which included intrinsic difference between the PS and P2VP Young's modulus, thin shell sphere with empty space model, and
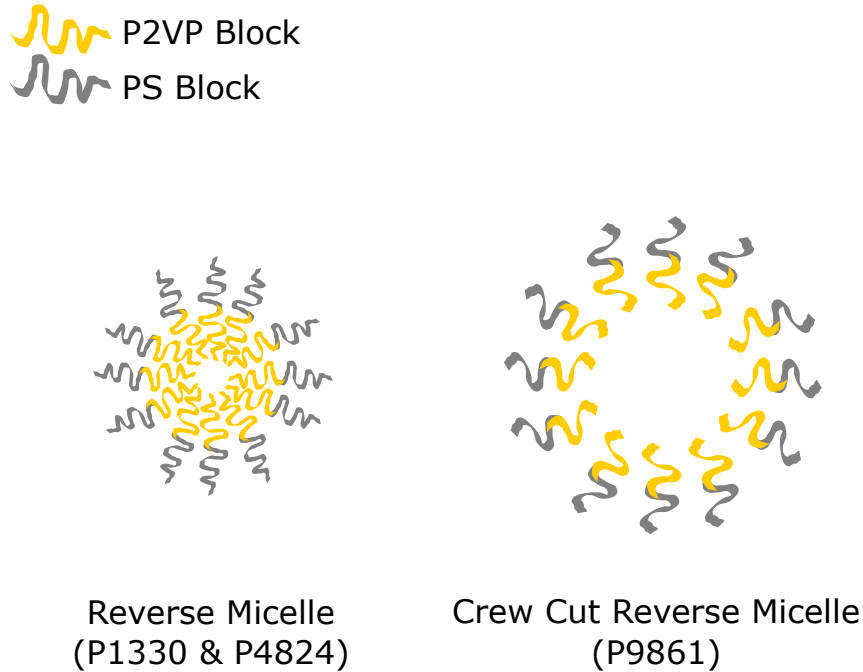
Figure 4.3: Representation of two different structures for micelles based on co-polymer relative length.

the effect of polymer orientation on Young's modulus measurements. A graphically representation of the three methods explored can be seen in Figure **4.4**.

4.5   Modelling

4.5.1   Intrinsic Differences

The first mechanism explored and presented in Figure **4.4 a.** was the differences being the result of intrinsic differences in the modulus of the co-polymer blocks. In this case, the AFM tip will first interact with the PS on the edge of the micelle, as such the Young's modulus would be dominated by PS. As the AFM tip continues across the micelle, it reaches the centroid and interacts with both the PS and P2VP blocks, where the Young's modulus would be a combination of PS and P2VP. Given the trend noted in Young's modulus across the micelle, if this model were to hold, the P2VP would have to have a significantly weaker Young's modulus than the PS to account for the decrease noted across the centroid.

   In addition to the trend across the individual micelles, we would expect the Young's
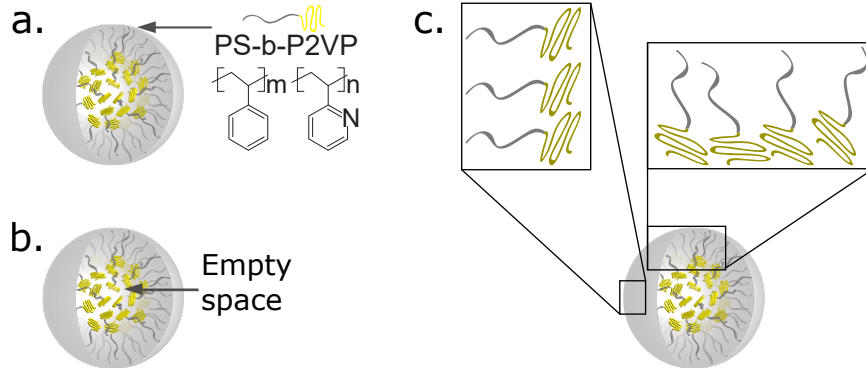
Figure 4.4: The three proposed reasoning for the Young's Modulus decrease through the micelle centroid

modulus of the micelle to trend with the molecular weight components of each of the co-polymers used. We would expect to see co-polymers with a larger relative component of PS to have a slightly stiffer Young's modulus.

In examining this model, we should first consider the elastic properties of both PS and P2VP individually. The literature finds the absolute values of the viscoelastic properties of PS and P2VP are are varied in both bulk and solution.[47] The results indicate that P2VP has a weaker modulus than PS, indicating that this model holds some weight.

Since there is a difference between the modulus of P2VP and PS, we can further examine this model by looking at the relative components of PS and P2VP in each type of micelle used. If we examine Table **4.1**, we can see the molecular weight components of each co-polymer. We can determine an approximate modulus for the core of each micelle by using the molecular weight to determine the percentage of PS and P2VP for each co-polymer. The percentage can be used to determine the portion of the literature modulus values that would contribute to the core modulus. The core to edge ratio can be determined by dividing our literature calculated core modulus by the literature values for PS. The calculated literature core to edge ratio are represented in **Figure 4.1 f)** as dots.

In examining **Figure 4.1 f)**, we can see that the P1330 and P4824 core to edge ratios fall within error to the ratio expected from literature. However, the ratio seen in P9861 fell far outside of the literature expected value. Given that this model can not explain the large drop in Young's modulus seen in P9861, it is seemingly not the correct model.

4.5.2 Thin Shell Model

The thin shell model is another mechanism we used that might explain the dip in Young's modulus based on modelling the micelle as an empty shell with space in the middle as seen in **Figure 4.4 b**. The general driving principle of this mechanism is the hypothesis that the centroid of the unloaded micelle is filled with either air or solvent. When the AFM tip interacts with the centroid, it would push into this cushion, leading to a reduction in the elastic modulus relative to the edges. The thin shell model is a widely studied mechanism and a variety of models and equations have been applied to similar systems. The models we tested are explained in **Table 4.2**.

To test the models shown in Table **4.2**, the P1330 co-polymer was used as a reference system to determine which model would best fit our data. In addition to the micelle diameter and shell thickness presented in **Table 4.1**, the Poisson's ratio, loading force, and deformation were also extracted from QNM maps and used as parameters in the modelling. The loading force and deformation were extracted from maps generated from their own channels in the same way the Young's modulus was extracted. **Tables 4.3 and 4.4** show the governing equations and how parameters were used in the calculations (move these tables to supporting?).

In order to determine which model best represented our system, we looked at the item studied, the equation, and how the parameters were used. The model that best represented our system would have studied a similar product, have an equation that closely resembles the DMT equation (**Eq. 4.1**, and require the least manipulation of parameters. We settled on the techniques used by Zhang *et al.* as they studied hollow spherical PS shells that seemed similar to our reverse micelles and required no further manipulation of parameters after extraction from the AFM maps. Additionally the governing equation Zhang *et al.* applied closely resembled the equation (**Eq. 4.3**) used for the DMT model (**Eq. 4.1** and **Eq. 4.2**). The Young's modulus is calculated in **Eq. 4.3** through the use of the sample's Poisson's ratio, ν, the loading force, F, the micelle radius, R, the sample deformation, d, and the shell thickness, h_s.

$$E = \frac{\sqrt{3(1-\nu^2)}}{4} \frac{FR}{dh_s^2} \tag{4.3}$$

Once the Zhang *et al.* model was determined to be the best fit for the P1330 system, we applied **Eq. 4.3** to all three co-polymers to accomplish a comprehensive analysis of our system. Two graphs were prepared tp analyze the changes in Young's modulus

Table 4.2: A summary of the thin shell models tested to describe the dip in Young's modulus across the centre of the micelle. All models were first applied to the P1330 toluene system before extended to the other polymers.

Item	Technique	Young's Modulus	Reference
Hollow PS Silica Spheres	-TM-AFM -Top of sphere located, substrate moved up and down -Thin shell model for elastic modulus measurement	2.70	[48]
Hollow Spherical Shells	-Piezoelectric-based resonant ultrasound spectroscopy -Spherical sample excited, natural frequencies observed -Governing equations extracted from Helmholtz Theorem and Spherical Bessel Equations	2.32	[49]
Spherical Polymer Brush (SPB)	-Molecular dynamics simulation -Soft-ball model -SPB represented by large elastic ball	2.10	[50]
Hollow Spheres (Ping Pong Balls and Expancel Spheres)	-Spheres were crushed between two plates to measure force and buckling	2.68	[51]

Table 4.3: A summary of the thin shell models equations used to describe the dip in Young's modulus across the centre of the micelle and where the parameters came from.

Item	Equation	Variables
Hollow PS Silica Spheres	$$E = \frac{\sqrt{3(1-\nu^2)}}{4}\frac{FR}{dh_s^2}$$	ν - used as 0.3 from QNM calibration F - extracted from QNM map d - extracted from QNM map R - extracted from SEM image h_s - extracted from SEM and TEM images
Hollow Spherical Shells	$$E = \omega(\sigma - \epsilon)^2$$	ω - extracted from the radius and shell thickness from TEM and SEM image $\sigma + \epsilon$ - stress and strain ratios extracted from the Possion Ratio, loading force, and deformation

Table 4.4: A summary of the thin shell models equations used to describe the dip in Young's modulus across the centre of the micelle and where the parameters came from.

Item	Equation	Variables
Spherical Polymer Brush (SPB)	$f_{SB}^{def} = \dfrac{Y}{4(1+\nu)}(\bar{I}_1+3)+\dfrac{Y}{6(1-2\nu)}(J-1)^2$	Y - represents Young's modulus $\bar{I}_1$ - first invariant of the isochoric part of the deformation tensor J - determinant of the deformation gradient - both the deformation tensor and deformation gradient were calculated using the micelle volume extracted from TEM, the micelle radius extracted from SEM, and the deformation extracted from the QNM map, and the force also extracted from the QNM map f_{SB}^{def} - was assumed to be 60 based on the study the equation came from
Hollow Spheres (Ping Pong Balls and Expancel Spheres)	$U_I = \dfrac{c_0}{4}\dfrac{Eh^{\frac{5}{2}}}{R}x^{\frac{3}{2}} + c_1\dfrac{Eh}{R}x^3$	U_I - energy term, extracted from force and deformation maps h - micelle thickness extracted from TEM and SEM images R - micelle radius extracted from SEM x - deformation extracted from QNM maps $c_0 + c_1$ - used as ν

30

first as a function of shell thickness and then as a function of micelle radius.

The first analysis we preformed was determining the Young's modulus based on the shell thickness while holding all other variables constant, the results of which can be seen in **Figure 4.5 a.**. To get the graph seen in **Figure 4.5 a.**, the Possion's ratio was set to 0.4, a standard value for PS based films and the value used by the Bruker AFM system, the loading force was set to 8.20 nN, the average value extracted from the Bruker modulus map for the P1330 system, and the deformation was set to 0.79 nm, the average value extracted for the P1330 from deformation maps captured alongside the modulus maps. The micelle radius was held constant at the increments noted in the legend of the figure and a range of curves were plotted. The average Young's modulus value for each type of micelle was determined by taking the average of the core and edge modulus and then plotted on the same graph as the ranging micelle radius curves. When analyzing the results seen in **Figure 4.5 a.** we can conclude that this model is a reasonable approximation for the trends seen in different micelles when we consider the average Young's modulus variations as a result of shell thickness and micelle radius. The micelle treatments fall within error of the curve that represents their micelle radius, indicating a reasonable approximation.

To further verify this model as a reasonable mechanism, we also applied it explain the variation seen between the core and corona. To accomplish this analysis we again used **Eq. 4.3** and held the same parameters constant as above. However, in this case we held the shell thickness constant at various increments which produced a range of lines. We plotted the Young's modulus values of the core and corona of each micelle as a function of the radius, which were extracted from the diameters noted in **Table 4.1**, on the same graph as the lines. The resulting graph can be seen in **Figure 4.5 b.** As seen here, the relationship between the core and corona Young's modulus can be loosely referred to as linear. However, none of the linear models closely approximate the relationship between each polymer. The maximum shell thickness noted in **Table 4.1** is the 14.96 nm of P9861. **Figure 4.5 b.** shows the P9861 values do not fall on the same linear model based on **Eq. 4.3** and is estimated to have a minimum shell thickness greater than 25 nm. In addition, this model also does not appear to work for P1330 and P4824. Our model indicates an anticipated shell thickness between 10 and 15 nm. This anticipated shell thickness far exceeds the values noted in **Table 4.1**, indicating this model and mechanism is a poor fit to describe the difference between the Young's modulus values of the core and corona.

It is possible that **Eq. 4.3** could be used with the parameters from the mapping for P9861 and P4824 to create a better linear fit for **Figure 4.5 b.** However, the loading force used by the Bruker AFM was constant in all tests runs and variations in the deformation was minimal between samples. It also seems unlikely that applying exact parameters for the samples in question would make any difference given how poor the fit for P1330 appeared in **Figure 4.5 b.**
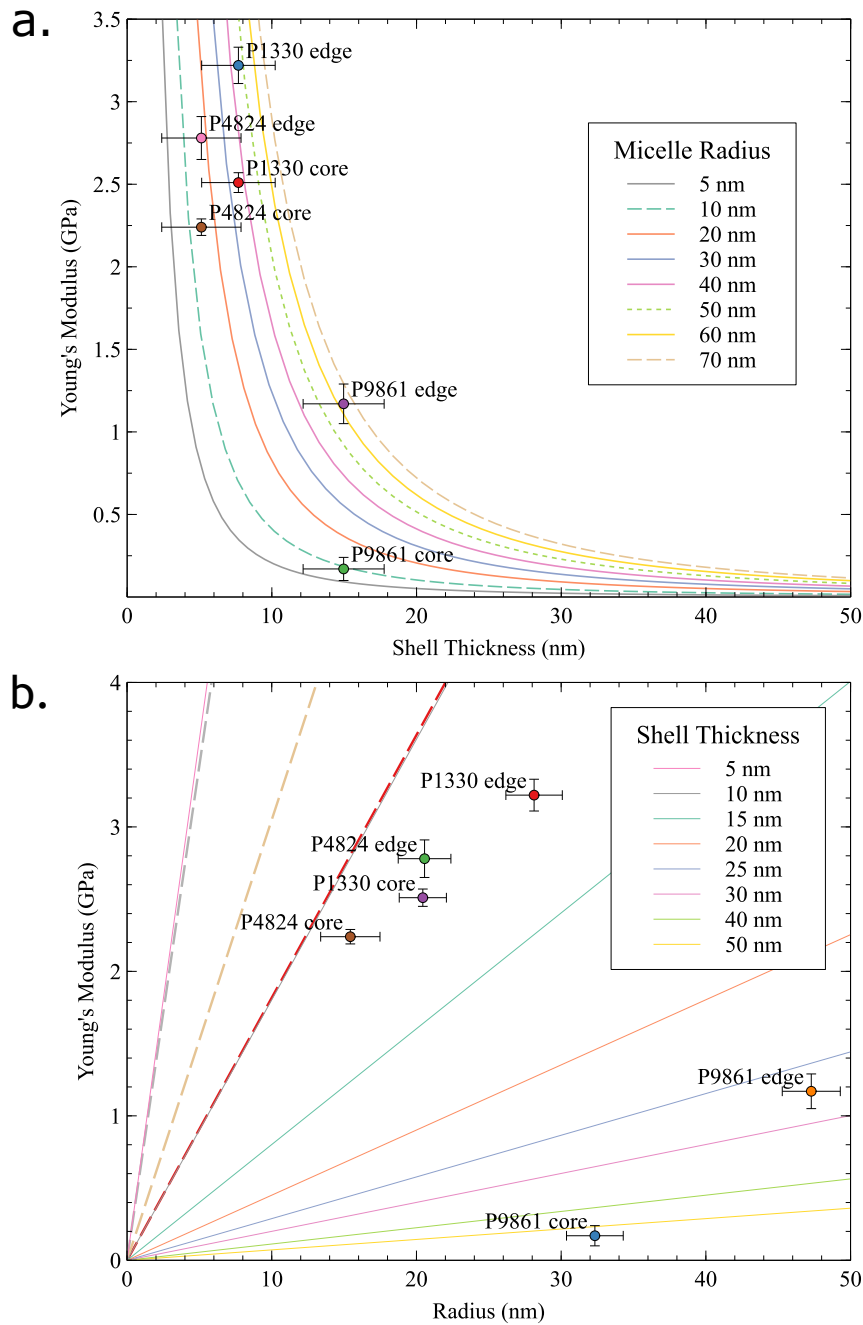
Figure 4.5: Modelling of the Young's modulus of using the thin shell model. Results indicate that this model may not be appropriate for describing the Young's Modulus decrease through the middle of the micelle.

4.5.3   Polymer Brush

The final mechanism proposed as a reasoning for the decrease of Young's modulus through the centre relates to the orientation of the co-polymer chains. As seen in **Figure 4.4 c.** one possible reasoning for the decrease in Young's modulus through the micelle centroid is due to the orientation of the co-polymer backbone. **Figure 4.4 c.** shows that along the outer edge of the micelle the AFM tip is interacting with polymer chains stacked in a horizontal lamellar structure as the AFM tip continues towards the center of the micelle the polymer chains begin to transition into a polymer brush structure. In the case of horizontally aligned co-polymer blocks, the AFM tip pushes down and the blocks have nowhere to move, potentially reinforcing the modulus. In the case of vertically aligned, polymer brush co-polymer blocks, the incoming AFM tip may deflect some of co-polymer blocks. If a co-polymer blocks where to be deflect by the AFM tip, it could prevent the tip from measuring it, leading to a reduced modulus when compared to the edges of the micelle. For this AFM tip interaction hypothesis and mechanism to hold true, the polymer brush must be found to have a decreased Young's modulus relative to the bulk modulus of a polymer.

The first step in analyzing this mechanism required proof that the orientation of polystrene blocks and crystals would effect the resulting elastic properties. After some research, cubic crystal elastic modulus values for polystrene were extracted and are presented in **Table 4.5**.[52, 53] The values presented in the first three columns of **Table 4.5** can be used in combination with the Zener ratio equation (**Eq. 4.4**) to determine the degree of anisotropy of a polystrene cubic crystal, A.[54] As noted, a value of one for the anisotropic ratio indicates an isotropic material, where properties such as the elastic modulus are the same in all directions.[54] The anisotropic ratio calculated for polystrene and noted in **Table 4.5** is 0.31, indicating that polystrene is an anisotropic cubic crystals and properties will vary depending on the orientation of the polystrene crystals.

Table 4.5: Cubic crystal elastic constants for polystrene and the resulting Zener ratio calculated using **Eq. 4.4**

c_{11}	c_{12}	c_{44}	A
9.10	3.78	0.83	0.31

$$A = \frac{2c_{44}}{c_{11} - c_{12}} \tag{4.4}$$

Further to confirming the difference of calculated elastic modulus depending on crystal orientation, we also examined the Young's modulus of polymer brush films. Multiple studies have been done examining the Young's modulus of polymer brushes. An interesting finding noted and explored in **Figure 4.6** is the concept of a critical segment length for polystyrene based polymer brushes. The critical segment length is defined as the minimum segment length beyond which a stable entanglement network begins to form.[55] In the case of bulk PS this segment length is known to be 31,000 g/mol.[55] As noted in **Figure 4.6**, both the P1330 and P4824 polymers have a PS molecular weight which exceeds the critical segment length. We can extrapolate this to indicate that the P1330 and P4824 micelle have more entanglements within the polymer chains of their micelles leading to an increase in modulus relative the the P9861 micelles. Further to the observation of a critical molecular weight for entanglements, the study also notes that the elastic modulus of a polymer brush will never reach the elastic modulus for bulk PS based on extrapolations of infinite molecular weight. The statement indicating that a polymer brush will have an elastic modulus less than its respective bulk film is supported by many other studies.[56, 57] Such a relationship between the polymer brush and bulk film modulus indicate that this mechanism appears to be the best fit when explaining the dip in Young's modulus between the edge and centroid of the micelle.

Additional studies of polymer brushes can also be used to confirm other trends noted in **Table 4.1**. One such study explored the effect on modulus of replacing longer chain lengths with significantly shorter chains. The results of this study showed a substantial decrease in modulus when the longer chains are replaced.[57] This can be used to describe the larger decrease in modulus when using the shorter chains of P9861. Any additional study noted the effects of stretched chains on modulus and found that longer stretched chains were more resistant to stress, indicating a higher modulus.[58] The relationship noted here can be used to describe the increase in Young's modulus between P1330 and P4824 as it appears the P1330 chains are stretched more than the P4724 chains based on the shell thickness. A further hypothesis was made to explain the increase in modulus between P1330 and P4824 as a result of the critical segment length of P2VP, however supporting literature could not be found.
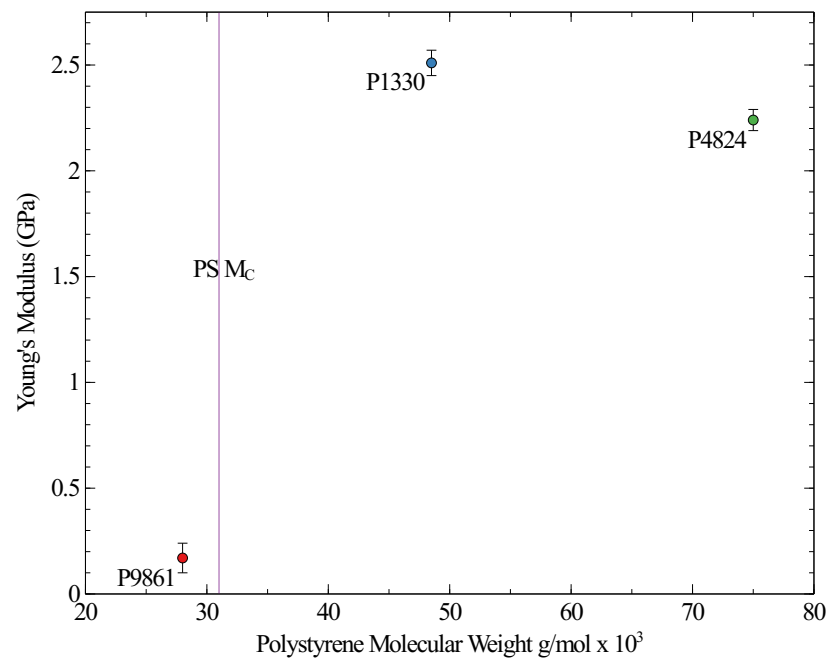
Figure 4.6: Measured core Young's modulus values plotted against the PS molecular weight (M_N). When the values are compared to the polystrene critical segment length (M_C noted in literature, it would appear the relative decrease in P9861 Young's modulus can be explained by being below the critical segment length.

4.6   Conclusion

This chapter explored the trends seen in the Young's modulus of the empty micelles. This was a necessary investigation as it allowed for the development of a mechanism to describe the decrease in Young's modulus in the centroid of the micelle. The most probably mechanism investigated was the polymer brush model, which indicated that weak entanglements between polymer brush strands lead to a decrease in the Young's modulus across the centroid. We can use this mechanism to provide reasoning for the increase in Young's modulus through the centroid when the reverse micelles are loaded with salts.

Chapter 5

Effect of Salt Loading on Young's Modulus - Iron Chloride

5.1 Introduction

Di-block co-polymer systems have been used to provide cost-effective bottom-up synthetic routes for fabricating nanoparticle arrays with high tunability and controllability in terms of size, shape, and spacing[6–8], owing to their two chemically different blocks which can lead to the formation of reverse micelles in selective solvents. If we incorporate proper metal precursors which usually possess higher affinity to the hydrophilic block, reverse micelles become a powerful method to synthesize nanoparticle arrays of metals, metals oxides, and metal alloys.[1, 8, 9]

Several types of di-block co-polymer reverse micelles have been employed for synthesizing nanoparticles with controllable sizes and spacings. A prime example of the usage of reverse micelles in this manner is generatation of size controled cadmium sulfide(CdS) nanoparticles via polystyrene-*block*-poly(acrylic acid) (PS-*b*-PAA) with different PS and PAA block lengths.[12, 13] The di-block co-polymer we examined in **Chapter 4**, polystyrene-*block*-poly(2vinyl pyridine) (PS-*b*-P2VP), has also been used to tailor the size and spacing of resultant gold(Au) nanoparticles by varying the lengths of P2VP and PS block.[14]

Additionally, the size of the resultant nanoparticles has also been tied to varying the amount of metal precursors with fixed block length of diblock copolymer PS-*b*-PAA[22],PS-*b*-P2VP[15, 23], polystyrene-*block*-poly(ethylene oxide) (PS-*b*-PEO)[24]

and polystyrene-*block*-poly(4vinyl pyridine) (PS-*b*-P4VP)[25]. The size of the nanoparticles depends on the amount of precursors that can be infiltrated into the micellar core whose size is determined by the length of the core block, thus providing a relatively large size controllability when using single di-block co-polymer with large block length[15].

Despite the size controllability, the amount of the precursor has a large impact on the order of the nanoparticle array due to the complex coordination and binding interaction between the micellar core block and the metal precursor. Literature has shown that the loading of $NbCl_5$ and $FeCl_3$ into PS-*b*-P2VP reverse micelles resulted in poor size distribution and dispersion of the resulted NPs above certain loading ratio.[26] A loading ratio of up to 1.0 of the $HAuCl_4$ was suggested to be the maximum loading of the PS-*b*-P2VP reverse micelles.[14] Other studies have indicated that the Fe^{3+} ions can hybridize with P2VP blocks mainly through intramolecular coordination, indicating the existence of the saturation loading of $FeCl_3$.[27] Therefore, a method to predict the threshold precursor loading of the reverse micelles could be helpful for developing an understanding of the interaction mechanisms during loading and improve the size controllability and order of the resultant nanoparticle array.

Furthermore, an understanding of interaction mechanism during the infiltration of the micelle core is of further interest, due to the ever-increasing complexity of the nanoparticle formulations, which rely on the reverse micelle technique.[6, 28] During multi-step loading the desired infiltration amount has been difficult to acheive.[28] Many nanoparticle formulations rely on a multi-step infiltration yet, there are very few methods available to confirm the infiltration of the precursor salts to the micelle core. Studies have shown that the infiltration of precursor salts will modify the nanomechanical properties of the reverse micelles, particularly infiltration has been shown to effect the elastic modulus of the reverse micelles.[28, 29] We suspect the elastic modulus to increase as the micellar core fills with precursor salts, leading to a harder micelle.

There exist a variety of techniques to measure the elastic modulus. Nanoindentation is one of the more common methods used to accurately and repeatedly measure the elastic modulus of polymer films.[30–32] However, nanoindentation relies on indentation depths on the order of the hundreds of nanometers to accurately measure the elastic modulus of the sample.[30–32] In our research, we are examining monolayer films of micelles with an estimated thickness of less than 50 nm. As such, nanoindentation

is not a suitable technique to confirm the change in elastic modulus due to the large size in indentation depth relative to the thickness of our micelle film. Further, typical nanoindentation techniques rely on mechanical or optical analysis of the contact area after indentation.[30, 33] The vast majority of polymers are quite soft, as such, minimal deformation is seen after indentation, leading to unreliable elastic modulus measurements.[30, 33]

However, atomic force microscopy (AFM) has proven to be a useful tool for measuring the nanomechanical properties of films through the use of the force-distance curves they can produce.[34] Tapping-mode AFM (TM-AFM) can be used to directly measure the elastic modulus of a sample by nanoindentation measurements, which differs from typical nanoindentation methods, as the indentation depths used are less than 10 nm.[28, 29, 35] TM-AFM has been used to confirm the loading of precursors into reverse micelles.[28, 29] Solmaz *et al.* used a TM-AFM and force indentation curves to analyze the elastic modulus of loaded reverse micelles.[28] They calculated the elastic modulus by indenting the AFM cantilever tip at the approximate centre of the reverse micelle to generate a force-indentation curve.[28] The sample's elastic modulus was extracted by applying a Hertz model to the loading region of the curve. However, it may not be capable of indicating the amount of precursor infiltration as it is challenging to verify that indentation measurements are taken above the centre of the loaded micelle core.[28]

TM-AFM can also be used to combine the topography and phases images to create a contour plot which can be related to the variation in mechanical properties as a result of changes to the composition of the film.[29, 35] The combination of phase and topography images has been used to confirm reverse micelle loading, but is incapable of quantifying the amount of salts loaded into the reverse micelle nanoreactor.

Recently, a new mode for AFM known as quantitative nanomechanical (QNM) mapping, has been developed, allowing users to map the topography and modulus of a sample simultaneously.[31, 32, 36] QNM modes work by fitting a model to the force-indentation curve generated by the AFM, allowing for the instantaneous mapping of mechanical properties.[31, 32, 34, 36, 37] Studies have shown that QNM AFM modes can reliably measure elastic modulus values for a variety of polymer films similar to those measured by more common nanoindentation techniques.[31, 32] Additionally, QNM AFM modes have been used to measure the nanomechanical properties of many soft materials including cells.[32]

Having now gained a deeper understanding of the unloaded micelles, we shifted our focus to the loading interactions. As above, loading interaction can be complicated and we wished to quanifty the interactions as we increased the amount of metal salt loaded. We chose the $FeCl_3$ system as it had been previously studied.[27] Sageshima *et al.* examined the morphological effects on the addition of $FeCl_3$ to a PS-*b*-P2VP film.[27] The study indicated an interaction between $FeCl_3$ and the P2VP film, with films conglomerating beyond a set loading ratio. The study also showed the $FeCl_3$ infiltration lead to stiffer polymer film.[27] We were interested in seeing if these relationships translated to the micellar system. We wished to connect the loading ratio to the Young's modulus and the size and order of the resultant nanoparticles. We were particularly interested in quantifying the relationship between the amount of precursor loaded and the change in Young's modulus.

5.2   Experimental Methods

Loaded solutions were prepared by dissolving 15 mg of the P4824 PS-*b*-P2VP co-polymer in 5 mL of toluene. The solutions were stirred for 24 hours at room temperature to form reverse micelles. After 24 hours, iron (III) chloride ($FeCl_3$; Sigma Aldrich) was added to the reverse micelles solutions to create solutions with a loading ratio of 0.05, 0.10, 0.15, 0.20, 0.30, 0.45, 0.60, 0.70. The loading ratio was determined based on the molar ratio of $FeCl_3$ to the P2VP block of the reverse micelle copolymer and is expressed in **Equation 5.1**. Solutions were stirred for an additional 24 hours at room temperature proceeding the salt addition to allow for the salts to infiltrate the core of the reverse micelles.

$$L = \frac{m_{FeCl_3} \cdot M_{PS-b-P2VP}}{m_{PS-b-P2VP} \cdot M_{FeCl_3} \cdot [VP]} \tag{5.1}$$

Proceeding infiltration, monolayer films of micelles were fabricated by spin coating at 2000 RPM for 45 s on clean silicon substrates and taken to an atomic force microscope (AFM) for quantum nanomechanical (QNM) mapping. Subsequently, in order to remove the micellar materials and yield the NPs arrays, the micelles coated substrates were exposed to radio frequency oxygen plasma(29.6W, 950 torrs, room temperature) which would also oxidize the iron precursors to form the iron oxide NPs.[59]

$FeCl_3$ loaded reverse micelles were also prepared by utilizing the homopolymer

poly(2vinyl pyridine)(hP2VP)(Mn: 77k g/mol, Polymer Source Inc) in combination with PS-*b*-P2VP, which was reported to be able to modify the lateral dispersion of the resulted NPs array.[26] In this route, the iron (III) chloride was mixed with 6 mg HP2VP in 1ml toluene in a vial while 15 mg PS-*b*-P2VP was dissolved in 4 ml toluene in a separate vial. After stirring for 72 hours, the above two solutions were mixed together so that it yielded the same PS-*b*-P2VP concentration as the direct loading, and the mixture was stirred for 7 days. The loading ratio was determined by the molar ratio of FeCl$_3$ to the 2VP units of hP2VP in this case and then two different loading ratio 0.30 and 0.53 were fabricated for further comparison.

To confirm the infiltration of the FeCl$_3$ we created hardness maps using a QNM AFM mode provided by the Bruker Nanoscope software. The elastic modulus for a loading ratio was determined by taking a line profile through 100 micelles by matching the coordinates in the topography channel to the elastic modulus channel. The resulting Young's modulus line profile was variable through the centre of the empty micelle. Due to the variability, the elastic modulus for each micelle was determined by taking the average of the centre points of the line profile. The number of points averaged to determine the modulus varied due to a range in the size of micelles measured. However, typically 10 points were taken. The modulus measurements for each micelle were fit using a Gaussian approximation to calculate the average modulus value and error for each treatment.

Literature indicates that the use of a sharp AFM tip will lead to substantial overestimates in Young's modulus.[32] As such, the final comparison of all treatments was done by taking the ratio of the Young's modulus loaded micelle to the Young's modulus of the empty micelle, hereafter referred to as the relative Young's modulus. The analysis was done based on the relative Young's modulus to minimize the impact of overestimated Young's modulus.

The nanoparticle height and polydispersity index analysis were determined from the AFM images. AFM images of the nanoparticle were extracted into WSxM where line profiles were taken from the topography maps. The peak height value was taken to be the height of the nanoparticle. In general, a hundred measurements on different particles within a $1\mu m$ x $1\mu m$ area were sampled to determine the average height and PDI from a histogram of the height distribution. The PDI was calculated by dividing the standard deviation by the mean of the data set.

The dispersion analysis of the AFM image was performed after extracting the x-y

coordinates of the nanoparticles. The x-y coordinates were determined by importing the AFM image into ImageJ. To find the coordinates of the particles, depending on the quality of the image, one of the following two processing options are chosen: the first is to binarize the image, and use ImageJ to calculate the location of each of the particles. If the noise level of the image is too high, or the binary image does not accurately represent the sizes of the cells, the size of the particles has to be found manually, by drawing an ellipse around the particles. The coordinates for the particles were extracted by running the analyze particle function in ImageJ.

The analysis was done using an in-house developed tool called the DisLocate package in Mathematica.[60] The pair correlation function (PCF) quantifies the positional order of intermolecular morphology. It describes the probability g(r) to find other particles at varying distances away from the centre of each particle, which is chosen as the origin to measure the distance from. A circular shell of width δr expands from the centre to a radius distance r. Any particles inside a circular shell of width Δr are counted over the radial spatial dimension. $g(r)$ is normalized by the density of the configuration, which then describes its deviation from of a hexagonal lattice, defined as the lattice disorder parameter. An entropic force map shows the planar probability map of first neighbour in relation to the centre particle by translating the particles to a common origin, which shows the degree of rotational symmetry of the system. A detailed description of the package and its other capabilities is described elsewhere.[60]

5.3   Results

5.3.1   Single Micelle Analysis

Figure 5.1 compares an empty micelle Young's modulus map to the $FeCl_3$ loaded micelle. **Figure 5.1 (c) and (f)** respectively show the line profile through a single unloaded and loaded micelle. As we recall from the empty micelle case, there is a dip through the centre of the micelle (**Chapter 4.4**). Once the micelle is loaded with precursor salt, the dip through the centre is no longer evident, it appears the loaded salt has reinforced the micelle through the centre.

The reinforcement through the centre can be related back to the mechanisms explored in **Chapter 4**. The first potential reasoning for the stiffening could be the incorporation of the salt into the micelle's centre cavity. Once the salt is driven inside
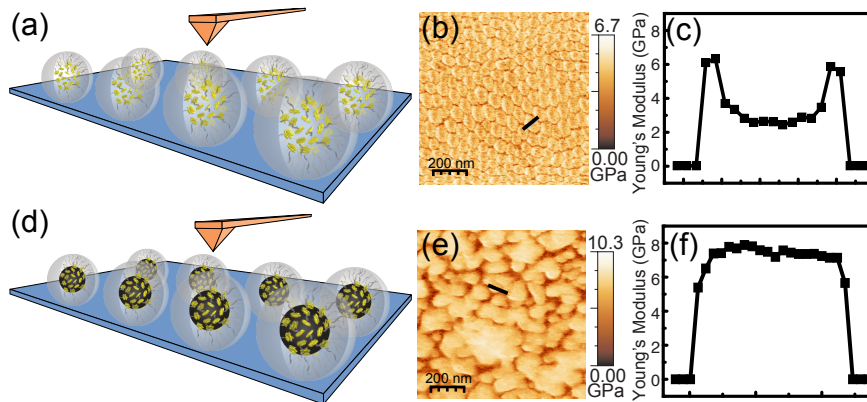
Figure 5.1: Schematic showing AFM procedure for quantum nanomechanimcal (QNM) mapping. The Young's modulus is mapped first for the unloaded micelles (a) and then the loaded micelles (d). AFM images (b, e) are analyzed by examining the line profile for each micelle (c, f).

the micelle, the AFM tip would interact with three materials through the centre (PS, P2VP, and $FeCl_3$) leading to an increase in the measured modulus. The loading interaction represented by this scenario relates to the thin shell model discussed in **Chapter 4.5.2**. If the $FeCl_3$ interacts in this manner, it would fill the empty shell, leading to an increase in the Young's modulus through the centre of the micelle.

Our second mode of interaction during loading could be an interaction with the PS leading to a stiffer polymer brush through the centre of the micelle. This interaction mode links back to the polymer brush model discussed in **Chapter 4.5.3**. If this mode holds true, we would suspect the $FeCl_3$ interaction with the PS would increase the linkages between the polymer brush like strands in the centre of the micelle. The increase in linkages would correlate to an increase in stiffness through the centre of the micelle.

Lastly, our salt could be interacting with the P2VP block, leading to a stiffening of the P2VP and an increase in the measured Young's modulus. This mode can be linked to the intrinsic difference mechanism discussed in **Chapter 4.5.1**. In this case, the stiffening of the P2VP would lead to an increase in relative Young's modulus between PS and P2VP. The change in the relative Young's modulus between the two co-polymers would lead to a decrease in the difference in Young's modulus between the edge and centre, appearing as the centre of the micelle hardening.

In all three cases, we would expect the an increase in the loading ratio would lead to an increase in the relative Young's modulus as the micelle would begin to stiffen

with increasing FeCl$_3$ addition.

5.3.2   Direct Loading

5.3.2.1   Micelle Analysis

Initial analysis for this system was done based on the one step direct salt loading approach. We first focused our attention on the reverse micelles and how they change as a result of loading. As seen in Fig. 5.2, we noted a degradation of the micelle film as the loading ratio increased as expected. At loadings between 0.1 and 0.2 (**Fig. 5.2 (b) and (c)**) the micelles can still be clearly differentiated. When the loadings are between 0.3 and 0.4 (**Fig. 5.2 (d) and (e)**), the micelles can still be seen but have begun to conglomerate in some areas. Once the loading exceeds 0.7 the film becomes conglomerate and individual micelles can not be distinguished (**Fig. 5.2 (f)**). The results we noted are similar to an FeCl$_3$ PS-*b*-P2VP lamella film studied by Sageshima which noted conglomeration at loading ratios above 0.6.[27]

The destruction of the reverse micelles with the increase of salt loading ratio suggests the application of the thin shell model (discussed in **Chapter 4**) does not explain the loading interaction of the FeCl$_3$ salt. In the case of the thin shell model, we would expect the infiltration to be dominated by osmosis, where the metal salts are pushed into the center of the micelle as they prefer the polar environment created in the micellar core. In this case the relative Young's modulus would increase with the increasing loading ratio (as noted in **Figure 5.3**), but we would expect the micelles to stay intact. The destruction of the micelles indicates that the FeCl$_3$ is interacting with one of the blocks of the di-block co-polymer causing the micelle to become unstable as the loading ratio increases.[27]
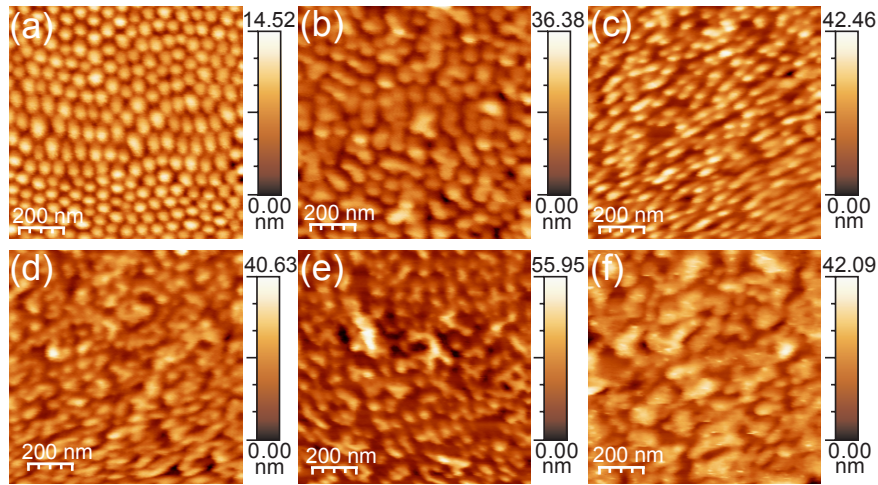
Figure 5.2: AFM images of PS-*b*-P2VP reverse micelles directly loaded with FeCl$_3$: (a) unloaded PS-*b*-P2VP, (b) loading ratio = 0.1, (c) loading ratio = 0.2, (d) loading ratio = 0.3, (e) loading ratio = 0.4, (f) loading ratio = 0.7. As the loading ratio increases, the reverse micelles begin to dissociate and form a conglomerate film.

5.3.2.2   Young's Modulus Analysis

Once we noted a destruction of the micelle as a result of the increasing salt loading ratio, we shifted our focus to the effect the direct salt loading has on the Young's modulus. **Figure 5.3** shows a plot of the relative Young's modulus against the loaded molar ratio of iron salt to P2VP block. We noted an overall trend that shows the increasing of Young's modulus with the molar ratio of iron salt. However, we differentiated three regions where the infiltration of the micellar core with FeCl$_3$ is dominated by different mechanisms.

In *Region I*, the relative Young's modulus is below one at low loading ratios, suggesting the Young's modulus of the sample is less than the empty micelles. We believe this behaviour could be due to the interaction of the FeCl$_3$ with the PS region of the di-block co-polymer. In these cases, the small quantity of FeCl$_3$ loaded may intercalate in the PS region leading to a slight increase in micelle size. Small amounts of intercalation between diblock copolymer components has been known to act as a plasticizer, leading to the lowering of the Young's modulus.[61, 62] The intercalation of FeCl$_3$ in the PS region can be linked to the polymer brush model discussed in **Chapter 4**. Incorporation of low levels of FeCl$_3$ in the PS corona can increase the swelling of the lamellar domain and decrease the tensile modulus.[61] Additionally, incorporation of small amounts of FeCl$_3$ into the PS decreases the PS polymer-polymer interactions.[62]
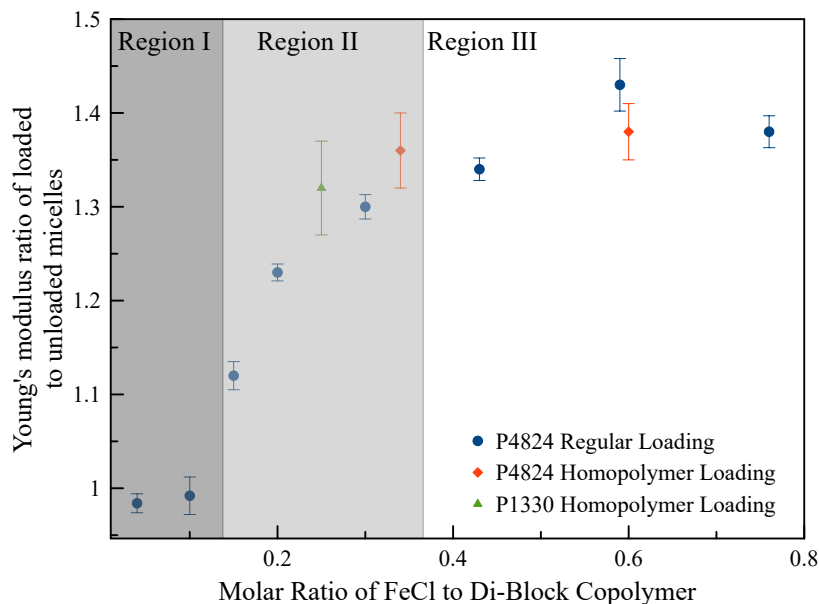
Figure 5.3: The relative Young's modulus (Young's modulus ratio of the loaded micelles to unloaded micelles) indicates a maximum infiltration at a loading ratio of approximately 0.4 (b). Use of the homopolymer appears to have lead to an earlier maximum infiltration. The homopolymer used in this study was the same block length, but used with the P4824 and P1330 polymer discussed in **Chapter 4.4**

A decrease in PS-PS interactions would lower the number of cross-linked polymer brush chains through the centre of the micelle, which would explain the decreased Young's modulus measured. In the study by Thompson, the nanoparticle addition was 15% of the co-polymer.[61] In *Region I* our loading ratio is less than 0.15, which would be equivalent to 15% indicating that this is the most probably mechanism in this region.

In *Region II* of **Figure 5.3**, increasing the loading ratio past 0.2 leads to a direct and sizable increase in the relative Young's modulus. We believe the increase in the relative Young's modulus in this region is a result of the $FeCl_3$ interacting with the P2VP block of the reverse micelle. As shown in **Figure 5.4**, we believe the $FeCl_3$ is incorporated along the backbone of the P2VP and cross-links adjacent P2VP chains. Incorporation of $FeCl_3$ along the backbone and between P2VP fits nicely with the intrinsic difference model discussed in **Chapter 4**. Incorporation of the $FeCl_3$ along the P2VP backbone and linkages between P2VP chains leads to a stiffening of the P2VP block.[27] As more salt is loaded and incorporated with the P2VP, the P2VP
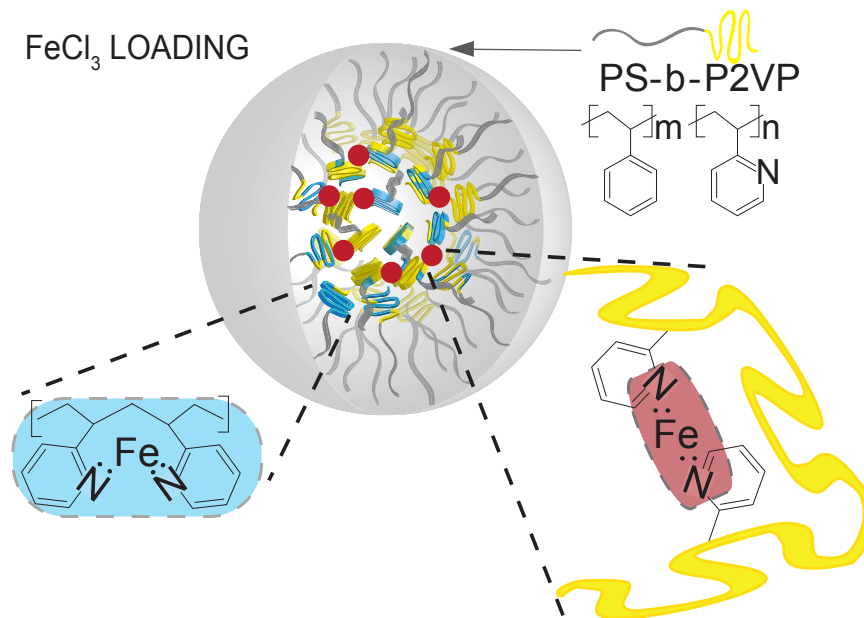
Figure 5.4: Schematic showing how $FeCl_3$ incorporates into the micellar core by binding along the P2VP block backbone and connecting adjacent P2VP blocks, leading to an increase in Young's modulus.

block becomes stiffer than the PS block. As the stiffness of the P2VP increases, so to would the Young's modulus through the centre of the loaded micelle.

In *Region II*, the $FeCl_3$ could interact with one or more lone pair electrons of the nitrogen atom in the 2VP unit through coordination interaction[63, 64]. Such polydentate interactions and also steric folding of the P2VP chains would result in limited loading of the iron precursors.

Lastly, *Region III* is where infiltration of the micellar core has reached a maximum. In this region, the relative Young's modulus begins to level out, further increases of the loading ratio leads to much smaller increase than in *Region II*. The start of *Region III* was determined based on the nanoparticle analysis discussed in **Chapter 5.3.2.3** In this region, the individual micelles become challenging to measure and the relative Young's modulus become more challenging to quantify accurately. As the loading ratio continues to increase, the micelles start to break down (as noted in **Section 5.3.2.1**). Within this region, we propose the P2VP block has become completely saturated with $FeCl_3$, and no further $FeCl_3$ can interact with the P2VP. One possible explanation is increasing the loading ratio beyond this point results in the incorporation of $FeCl_3$ in the PS corona and leads to the unravelling and conglomeration of the reverse micelles.

Table 5.1: Summary of nanoparticle height and polydispersity index for each $FeCl_3$ loading ratio.

Loading Ratio	Average Height (nm) ± SD	PDI	Nearest Neighbour Distance (nm)	Lattice Disorder Parameter
0.05	6.5 ± 0.7	0.1	49.8	12.6
0.10	6.0 ± 1.5	0.3	49.7	32.0
0.15	7.2 ± 0.7	0.1	44.7	21.9
0.20	7.1 ± 2.6	0.4	41.1	20.9
0.30	11.0 ± 3.2	0.2	35.8	17.5
0.45	12.8 ± 2.7	0.2	34.7	30.1
0.60	8.1 ± 2.0	0.3	34.1	28.3
0.70	9.5 ± 4.7	0.3	33.5	27.6
P1330-HP2VP(0.30)	4.06 ± 1.02	0.22	59.8	17.3
0.34-HP2VP(0.30)	3.53 ± 0.75	0.21	56.9	11.0
0.60-HP2VP(0.53)	6.30 ± 1.66	0.26	65.8	20.3

This region can also be related to **Figure 5.4**. As the amount of $FeCl_3$ increases it complexes directly on the P2VP chain.[27] More incorporation of the $FeCl_3$ along the P2VP backbone makes the micelles more unstable leading to the destruction noted in **Section 5.3.2.1**.[27]

5.3.2.3 Nanoparticle Analysis

Further analysis was done to connect the relative Young's modulus and loading ratio to the resultant nanoparticle size and array. **Table 5.1** shows how the particle height and array disorder change as a function of the loading ratio. We can connect the particle size and array disorder to the regions noted in **Figure 5.3**. In *Region I* the resulting particles stay at approximately a constant size as the loading ratio increases. The resultant arrays also have particles at a similar distance to each other.

In *Region II*, the particle size begins to increase with the loading ratio and relative Young's modulus. In this region, the nearest neighbour distance decreases as does the lattice disorder parameter. The trends noted here illustrate that in *Region II* the particle size and array order can be successfully tuned by the loading ratio. In this region, the relative Young's modulus could be used to predict the particle size and lattice disorder.

In *Region III*, we can see that all particle parameters listed in **Table 5.1** become more variable. In this region, the particles are closely packed relative to the other treatments. The lattice disorder in this region also increases relative to *Region II*. In this zone, it is difficult to use the relative Young's modulus to predict or model any parameters of the resultant particle array.

5.3.3 Homopolymer Loading

With a moderate understand of the direct loading systems, we expanded the experiment to see if a more complex loading systems would yield similar results but with better particle order. Shan noted homopolymer poly(2vinyl pyridine)(HP2VP) could act as carriers to bind metal precursors for the subsequent loading of PS-*b*-P2VP reverse micelles with similar molecular weight P2VP block and improve the order of the nanoparticle arrays under certain loading ratios.[26]

In this experiment, the $FeCl_3$ is complexed on to the HP2VP block before it is loaded into the reverse micelle solution. After the HP2VP is complexed with $FeCl_3$ and loaded into the reverse micelle solution, there are two potential processes for the loading of the reverse micelle. One process involves the filling of the micelle core with the complexed HP2VP. This mechanism would relate back to the thin shell and intrinsic difference mechanisms discussed in **Chapter 4**. In the case of the thin shell mechanism, the micelle core would be full of a stiffer material. The Young's modulus through the centre would be dominated by the stiffer material. In the case of the intrinsic difference mechanism, incorporating more, stiffer P2VP blocks into the centre of the micelle would shift the ratio to favour the Young's modulus of the stiffened P2VP. In both of these cases, we would expect the Young's modulus to increase proportionally
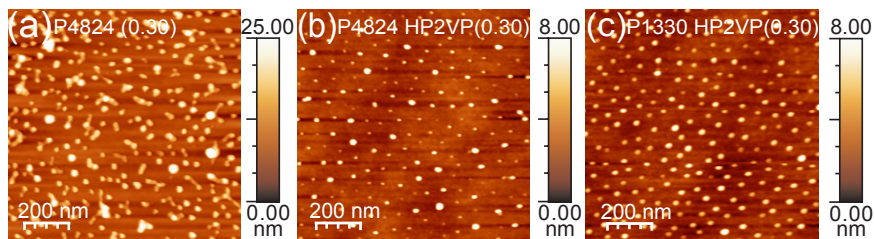
Figure 5.5: AFM images of single layer iron oxide nanoparticles with different loading conditions. (a) 0.3 loading ratio P4824 direct loading, (b) 0.3 loading ratio HP2VP assisted P4824 loading, (c) 0.3 loading ratio HP2VP assisted P1330 loading.

with the amount of HP2VP loaded into the system. We can think of this process as the addition of loaded P2VP chains to the the reverse micelle. For example, if our typical micelle has 100 P2VP chains this process would add additionally chains that are partially loaded leading to a micelle which has greater than 100 P2VP chains.

The second process involves the exchange of P2VP blocks. When the complexed HP2VP is loaded into the reverse micelle solution, it would exchange places with the unloaded P2VP blocks in the micelle core. This process would result in measured interactions similar to those in *Region II* of the direct loading graph. Here, the change in Young's modulus is the result of the stiffening of the P2VP blocks leading to a change in ratios for the intrinsic differences mechanism. This loading of the reverse micelles would increase proportionally with the amount of $FeCl_3$ loaded onto the HP2VP. Using the same example as above, in this case the number of P2VP chains in a reverse micelle would stay constant at 100, but the unloaded chains would be removed as they are replaced with loaded chains.

In comparing the homopolymer results to the direct loading with 0.30 loading ratio, the solution of 0.30 HP2VP loading ratio (0.34 loading ratio relative to vinyl pyridine units in PS-*b*-P2VP) yielded more ordered arrays of NPs after oxygen plasma etching according to the lattice disorder parameter shown in **Figure 5.5** and **Table 5.1**. As indicated in **Figure 5.3**, the relative Young's modulus of the micelles is larger than 1.3 in this case, similar to that of the direct loading with 0.30 loading ratio. However, the NPs are much smaller with 3.53 nm average height while the direct loading with 0.30 loading ratio results in NPs with 11.08 nm average height. Despite the smaller size, the homopolymer loaded micelles create a more order nanoparticle array after loading **Figure 5.5**.

As discussed earlier, the $FeCl_3$ could be interacting with one or more lone pair electrons of the nitrogen atom in the 2VP unit through coordination interaction[63, 64]. Such polydentate interactions and also steric folding of the HP2VP chains would result in limited loading of the iron precursors, which could lead to the smaller effective iron salts infiltration relative to direct loading, considering the limited space in the micellar core. In addition, the HP2VP itself could occupy the available space inside the micellar core as well. Both processes could likely be the explanation of the nanoparticle size reduction using homopolymer loading and link to the previously discussed mechanisms for loading.

Two solutions of 0.3 loading ratio of HP2VP were prepared and were loaded into

a solution of P1330 and P4824 micelles. The loading ratio was recalculated for the total number of P2VP chains and was plotted against the relative Young's modulus presented in **Figure 5.3**. The results showed the P1330 loaded micelles had a lower relative Young's modulus than the P4824 micelle. However, the nanoparticle height and array parameters showed no major differences between the two treatments.

Another solution of 0.53 HP2VP loading ratio (0.60 loading ratio relative to vinyl pyridine units in PS-*b*-P2VP) was also synthesized to study the impact of different $FeCl_3$ loading ratio on HP2VP loading. In this case, the Young's modulus ratio of the micelles is similar to that of 0.30 HP2VP loading ratio as shown in Figure 5.3, indicating that the maximum precursor infiltration has been already reached. In addition, agglomerations of the NPs appears with low order dispersion after oxygen plasma treatment, which could be the reason why the average height of the NPs shifts upward to 6.30 nm relative to that of 0.30 HP2VP loading for the similar Young's modulus ratio of the loaded micelles. The results of different HP2VP loading ratios suggest that the maximum $FeCl_3$ loading occurs at around 0.30 HP2VP loading ratio. Increasing the loading ratio further results in poor lateral dispersion and size distribution of the NPs.

In examining **Figure 5.3** we can connect the differences between the homopolymer loadings and reverse micelle co-polymers to determine which proposed loading mechanism best describes this system. First we can compare the relative Young's modulus of the 0.3 homopolymer loading of the P4824 to the equivalent projected direct loading value of 0.34. In this case, the measured value for the homopolymer loading was found to be 1.1 times greater than the projected direct loading value. These results indicate the loading process is most likely dominated by the exchange of P2VP chains. In **Chapter 4.5.1** we showed that P2VP had a lower Young's modulus than PS. Incorporating more partially loaded or unloaded P2VP chains in the core should lead to a relative Young's modulus less than the direct loading regime, as a greater portion of the Young's modulus in the centroid would be coming from unloaded P2VP chains. However, we see an increase relative to the projected direct loading value, indicating that the HP2VP is most likely more effectively stiffened during the homopolymer loading.

We can also examine the two P4824 homopolymer loaded cases. In all loading cases, 4 ml of reverse micelle solution was added to 1 ml of homopolymer solution which contained 6 mg of homopolymer loaded with the $FeCl_3$. For these two treatments,

the relative Young's modulus is about the same. However, the resulting nanoparticles have almost doubled in size. As discussed earlier in this chapter, the relative Young's modulus appears to level out in *Region III*. The 0.54 homopolymer loading fails well within this region. It is therefore difficult to use this point to confirm which loading procedure is most accurate, as the minimal difference between the two loadings could be a result of having reached the maximum $FeCl_3$ infiltration or a result of the homopolymer dominating the change in relative Young's modulus. However, we believe the minimal change is a result of the loading trend for $FeCl_3$ holding with the homopolymer loading, indicating a maximum effective loading.

We can also analyze the differences between the P1330 and P4824 loading cases. Here, the homopolymer was loading ratio was 0.3 for both copolymers. In this case, the loading ratio was recalculated for the total molecular weight of the P2VP blocks and presented in **Figure 5.3**. The total molecular weight of the P2VP for the P1330 system (147,000 g/mol) was less than that of the P4824 system (143,500 g/mol) leading to a lower effective loading in the P1330 system. The results show that the relative Young's modulus is inversely proportional to the total M_N of our loaded system and proportional to the total M_N adjusted loading ratio. These results again favour the P2VP exchange mechanism.

5.4   Conclusion

In exploring the loading of $FeCl_3$ into PS-*b*-P2VP reverse micelles, we were able to develop an understanding of the interaction that lead to the increased Young's modulus. The $FeCl_3$ seems to act as a binder and stiffener for the modelled polymer brush in the centre of the micelle. Additionally, we were able to develop a loading curve as a function of loaded molar ratio. The loading curve seems to hold regardless of the complexity of the loading for this particular salt. Further experiments should be preformed to determine the universality of this curve and the results represented on it.

Chapter 6

Effect of Solvents on Young's Modulus

6.1 Introduction

Solvents have been studied as a way to tune the morphology of polymer films. Polymer size and concentration, film deposition rate, and solvent type have all been linked to the composition of polymer films.[16, 17] Theoretically, the degree of polymerization of a co-polymer can lead to the expression of varying morphologies and can also effect the corona thickness to core radius ratio.[17] Varying morphologies have also been noted experimentally as a function of dip coating rate and solvent.[16] Here, it was noted that different solvents will produce larger micelles but at different dip coating rates.[16] The exhibition of various morphologies for block co-polymers has further been explored as a function of the percent weight of solvent used.[18]

The production of various morphologies seems to be linked to the properties of the solvents used. Studies have indicated that solvents can have varying swelling parameters, cross-links densities, and Flory-Huggins parameters.[19–21] The cited parameters have been linked to the volume and size of polymer films but have not been extensively used to study the mechanical properties.

Though solvents have been widely cited as a way to tune the morphology of polymer films, limited research has been done on how solvents effect the mechanical properties of polymer films and micelles. In the case of micelles, it has been hypothesized that variations in solvents could lead to an increase in interfacial energy between the solvent

and the core block, increasing the stretching of the core block and leading to larger micelles.[10]

This chapter looks to examine and quantify the effects toluene a o-xylene have on the mechanical properties of the reverse micelle loading system.

6.2   Experimental Methods

Di-block co-polymer of poly(styrene-b-2-vinyl pyridine) (PS-b-P2VP) (P1330) was dissolved in toluene or o-xylene with a concentration of 3 mg/mL. The micelles solution was stirred for 24 hr. After confirmation of spherical micelles formation with Atomic Force Microscopy (AFM), non-hydrated lithium hydroxide (LiOH) (Merck) was first added and stirred for 48 hr, the solution was centrifuged to remove excess salt. Hydrofluoric acid (HF, 48%) was added and stirred for 24 hr. The final LiOH-loaded micelles solution was taken with AFM.

Samples for QNM were created at the end of each loading step by spin-coating μL of the co-polymer solution on a silicon substrate. A BioScope Catalyst AFM (Bruker; Billerica, Massachusetts, USA) was used for the QNM imaging. The Young's modulus and topography was imaged for all sample. The complete set of loadings was imaged for each solvent in the order of unloaded micelles, LiOH loaded micelles, and LiF loaded micelles. Young's modulus value was extracted by taking a line profile through which ran through the center of the micelle (reference figure). One hundred line profiles were taken and normalized to determine the average Young's modulus value for each loading stage and solvent. The Young's modulus for both loading stages was divided against the Young's modulus for the unloaded micelles to determine and Young's modulus ratio. The Young's modulus of the micelles was further examined to determine if a hardness difference existed between the micelle corona and core. One hundred points were taken at both the edge and center of the micelles. Points were normalized to determine the average Young's modulus of each micelle zone. A Young's modulus ratio for the micelles in each solvent was determined by dividing the hardness of the core by the hardness of the corona.

Transmission electron microscope/Scanning transmission electron microscope(JEOL 2010F TEM/STEM) operating at 200kV was applied to check the size of the staining micelles. The carbon coated copper grids were dipped into the micelles solution to form a thin layer of micelles, which allowed the direct TEM/STEM characterization

of the individual micelle. In order to observe the size different of micellar cores(P2VP domains) in different solvents, TEM grids with micelles were exposed to I_2 vapour for 3 h at room temperature to selectively stain the P2VP cores, by placing iodine crystals and TEM grids in a closed glass container.

Image J was used to extract the size information of iodine stained micellar cores from the STEM images by drawing binarizing and manually picking the particles. In order to acquire a statistical diameter representation of micellar cores, more than 100 micellar cores of P1330 in o-xylene and 70 micellar cores of P1330 in toluene were randomly selected in the STEM images1. Furthermore, the gaussian fitting was also performed to minimize the effect of some extra small and large outliers.

WSXM was used to measure the height of the resulting nanoparticles by drawing a line profile through individual nanoparticles. To acquire a statistical height representation of nanoparticles, 100 particles were randomly selected in the AFM images1. More reliable statistical height values were obtained using gaussian fitting to minimize the effect of some extra small and large outliers.

Analysis of the order of the resultant nanoparticle array was performed using an in-house developed tool known as disLocate.[60] The parameters used in this analysis include the pair correlation function and coordination number. The pair correlation function (PCF) quantifies the translational order of intermolecular morphology. It describes the probability g(r) to find other particles at varying distances away from the centre of each particle, which is chosen as the origin to measure the distance from. A circular shell of width dr expands from the centre to a radius distance r. Any particles inside a circular shell of width Δr are counted together and binned to produce the neighbour probability n_n(r) as a function of distance. g(r) is normalized by the density of the configuration ρ, which then describes its the deviation from of an ideal gas.

Coordination number of neighbours is as defined by number of Voronoi facets using the Voronio tessellation, which is the number of neighbours to which the object is bonded. The Voronoi tessellation partitions the substrate into sections by using the centroids of the particles. Each tile is defined by the set of perpendicular bisecting lines that defines an equal distance between objects and occurs at the midpoint of the line directly connecting the central particle to its neighbours. This procedure produces localized partitions that express the maximum space each molecule can potentially posses. The local coordination number takes on discrete values, allowing for each value to be represented by a unique colour. Each particle has a unique colour that is distinct

and easily differentiated from the other possible values.

6.3   Results

Co-polymer block length has been known to effect the micelle size and entropy of a reverse micelle system.[10] Small co-polymer block lengths can lead to instability, which could be used to describe the ballooning effect and extreme decrease of Young's modulus noticed in the polymer denoted 9861 and discussed in **Chapter 4**. An interesting finding from one such study stated that the relationship between the core block length and core radius is weak and hypothesized that the weak relationship is a result of low interfacial energy between the core block and solvent used. They hypothesize that an increase interfacial energy between the solvent and the core block would lead to a larger micelle with increased stretching in the core block.[10].

We attempted to use this finding to describe the strange behaviour of the P9861 co-polymer micelles but were unsuccessful in our application. We believe our lack of success stemmed from our inability to directly correlate the P9861 reverse micelles with a resultant nanoparticle.[65] It seems the loading of the P9861 reverse micelles are inconsistent and require a deeper theoretical and experimental analysis.

We did find the hypothesis related to a change in interfacial energy to be fascinating. We hypothesized that if increased stretching is the cause of the large micelles, we would expect to see stiffer unloaded reverse micelles. We were curious as to how this change in stiffness of the unloaded micelles would effect the loading and opted to analyze the P1330 and P4824 co-polymers as they were know to create nanoparticle arrays with a 1:1 ratio of reverse micelles to resultant nanoparticles.

6.3.1   Solvent Comparison

Figure 6.1 compares the modulus and topography maps of the P1330 micelles created in toluene and o-xylene. The micelles presented display a similar topography, where the o-xylene micelles are slightly swollen compared to their toluene counterparts, as noted in **Table 6.1**. However, the modulus of the o-xylene micelles is stiffer at both the edges and centre as evident from the line profile comparisons and the modulus parameters presented in **Table 6.1**.

TEM analysis of the o-xylene cores was undertaken to help understand the increase
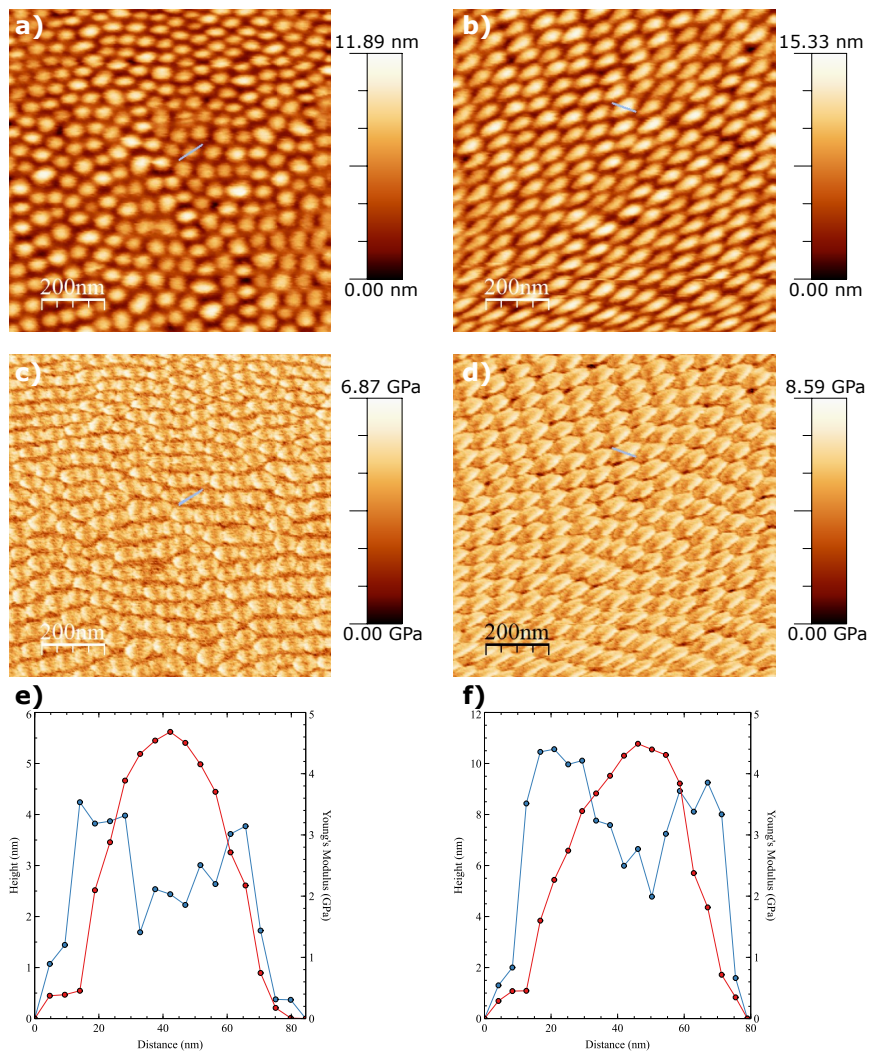
Figure 6.1: A comparison of the AFM topography and Young's modulus maps of the P1330 reverse micelles created in toluene and o-xylene. The o-xylene micelles appears to be slightly stiffer through the centre.
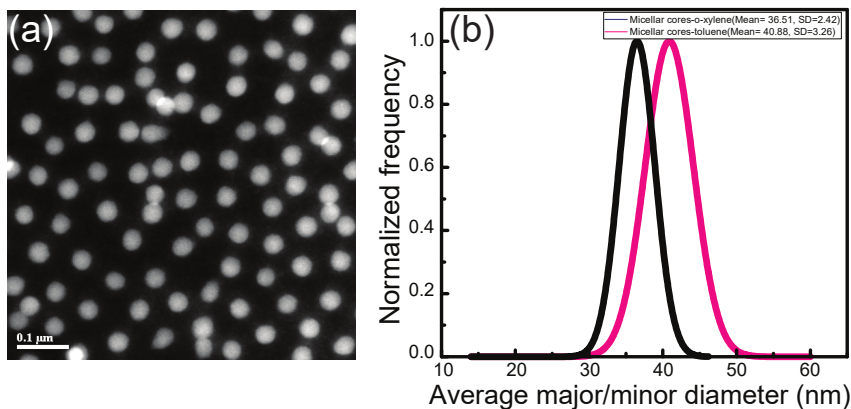
Figure 6.2: A sample TEM image used to determine the core radius of the reverse micelles made using each treatment. The resultant Gaussian shows the o-xylene micelles had a smaller core diameter.

in Young's modulus. A sample TEM image and the resultant Gaussian fit of the toluene and o-xylene cores can is noted in **6.2**. The result showed the o-xylene micelles have a smaller core diameter than their toluene counterparts.

The corona thickness was calculated by subtracting the micelle diameter from the core diameter. These measurements are presented in **Table 6.1**. The results show that the o-xylene micelles have a larger corona thickness than the toluene micelles.

When this analysis was repeated with the P4824 reverse micelles, the results were similar to those noted in P1330. The o-xylene created larger micelles with a thicker corona the Young's modulus was increased. We noted that the increase in the overall size of the micelle and the corona thickness correlated with the amount of PS in the co-polymer. The P4824 exhibited a greater swelling as it has a larger relative amount of PS than the P1330.

Table 6.1: Full examination of the reverse micelles lead indicates that the use of o-xylene lead to a reverse micelle which was stiffer and had s larger corona.

	Tol 1330	O-Xy 1330	Tol 4824	O-xy 4824
Micellar Diameter (nm)	56.26 ± 3.90	65.32 ± 3.74	41.12 ± 3.64	55.06 ± 3.52
Core Diameter (nm)	40.88 ± 3.26	36.51 ± 2.42	30.86 ± 4.10	28.48 ± 2.21
Corona Thickness (nm)	7.69 ± 2.54	14.41 ± 2.23	5.13 ± 2.54	13.29 ± 2.23
Micelle Core Young's Modulus (GPa)	2.51 ± 0.06	2.76 ± 0.17	2.24 ± 0.05	2.55 ± 0.13
Micelle Edge Young's Modulus (GPa)	3.22 ± 0.11	3.43 ± 0.15	2.78 ± 0.13	3.04 ± 0.18

6.3.2   Connection to Models

To explain the increase in modulus as a function of solvent, the results represented in **Table 6.1** were connected to the models presented in **Chapter 4.5**.

6.3.2.1   Thin Shell Model

The first model we connected the solvent results to was the thin shell model presented in **Chapter 4.5.2**. The best fit model used **Equation 6.1** as the governing equation. Where the Young's modulus, E is calculated through the use of the sample's Poisson's ratio, ν, the loading force, F, the micelle radius, R, the sample deformation, d, and the shell thickness, h_s.

$$E = \frac{\sqrt{3(1 - \nu^2)}}{4} \frac{FR}{dh_s^2} \tag{6.1}$$

Figure 6.3 shows the application of the thin shell model to the P1330 measurements presented it **Table 6.1**. However, unlike **Chapter 4.5.2**, only the micelle radius and shell thickness were held constant at their measured value. In **Figure 6.3 b)**, the shell thickness is held constant for the different solvents and the sample deformation and loading force were varied to fit **Equation 6.1** to our data points. The deformation and

loading force retrieved from this fit were within error of the experimentally determined values. The results of fitting **Equation 6.1** to the shell thickness showed that the thin shell model is a reasonable approximation for the differences between the edge and core of both types of micelles.

However, our results do not seem to follow the trend represented when the micelle radius is held constant. In this case, the micelle radius for both micelles is approximately 30 nm. The trend represented in **Figure 6.3 a)** claims that for similar micelle radii, the Young's modulus should decrease as the shell thickness increases. Our results indicate that the Young's modulus is increasing as the shell thickness increases, indicating the thin shell model may not describe the difference between the two solvents effectively.
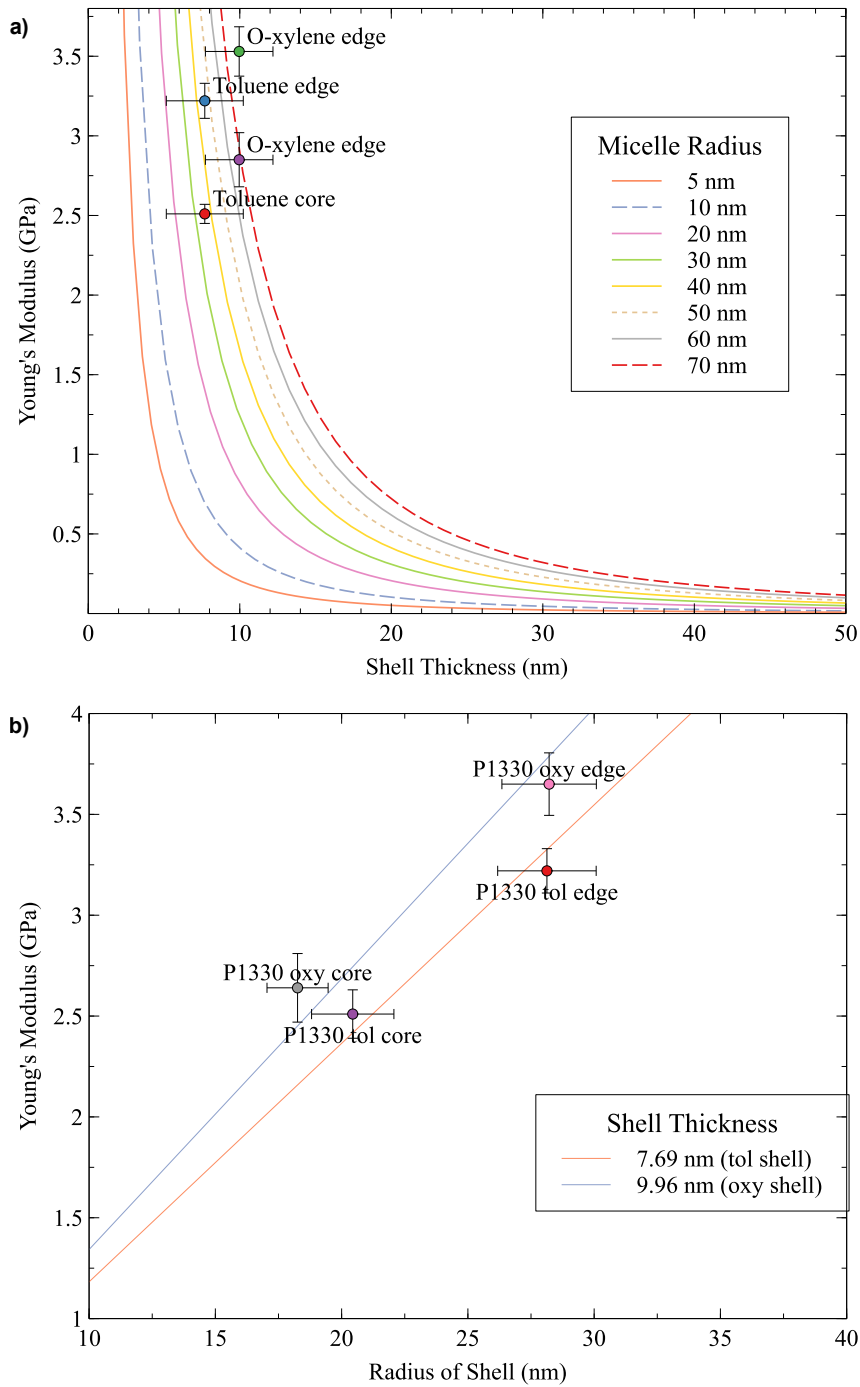
Figure 6.3: The thin shell model was applied to this solvent system. In this case, holding the radius constant does not properly represent this model. However, **Equation 6.1** can be fit within error to model the dip seen.

6.3.2.2 Polymer Brush Model

We could also examine the differences in solvents as an aspect of the polymer brush model. As noted in the results, we see that the core to edge Young's modulus ratio has decreased for the o-xylene loaded micelles, which indicates that the Young's modulus drop in the centre is greater than in the o-xylene case. We also noted that the overall values appear to be stiffer in the case of the o-xylene. These facts both seem to indicate that o-xylene is a better solvent for the PS block. We believe the change in core to edge Young's modulus ratio is a result of increased PS swelling and decrease linkages between PS blocks in the o-xylene.

These hypothesis both seem to be verified by the literature. Literature indicates that o-xylene has a slightly larger swelling parameter than toluene for a PS-vinylbenzene di-block micelle. Additionally, o-xylene has a lower cross-link density than toluene for the same PS-vinylbenzene di-block micelle.[19] Additionally, the results presented in **Table 6.1** show that the o-xylene create a larger micelle when compared to the toluene solution.

However, **Figure 6.3 b)** shows that there is a steeper decrease between the edge and centre in the o-xylene micelle. The lower cross-link density for the PS-vinylbenzene di-block co-polymer o-xylene explains the steeper decrease in the micelle.

6.3.2.3 Intrinsic Differences Model

Lastly, we can apply the solvent data to the intrinsic differences model. In the application of this model, we would expect the o-xylene to be a better solvent for the PS and potentially P2VP block of the micelle. In this case, the Young's modulus increase would be due to the co-polymer blocks swelling more in the o-xylene than the toluene. We would expect to see a difference in the swelling power of the solvents.

The swelling power for PS in toluene is stated as 2.01 whereas the swelling power for PS in o-xylene is stated as 2.02.[20] Our results show that the o-xylene micelles have swelled more than their toluene counterparts, providing proof of the increased swelling parameter.

Overall, it seems that components of all three models can be used to describe and understand the effect of solvents on the reverse micelles.

6.3.3   Effects on Loading

Before we can discuss the differences between the solvents, we must first understand the method of infiltration. For this study, we focused on the formation of lithium fluoride nanoparticles from a lithium hydroxide precursor. The reverse micelle nanoreactor is a common method used for the formation of lithium fluoride and we were interested in examining similarities to the iron chloride system.

The use of the lithium fluoride system was primarily motivated by the differences in interaction methods. In the case of iron chloride, we believe the $FeCl_3$ is complexing on the P2VP block. However, unlike the iron chloride system there is no evidence of an interaction between the P2VP block and lithium hydroxide. RAMAN and FTIR analysis have shown no difference between the unloaded micelles and LiOH loaded micelles. The lack of evidence for an interaction between the LiOH and P2VP block was taken to mean the method of infiltration was osmosis driven.

Furthermore, we wished to avoid the iron chloride system as the complexation of the $FeCl_3$ onto the P2VP seemed to be a more complex system. We were unsure if the increased micelle size and change in surface area of the P2VP block exposed to the solvent would change the effective loading ratio of the $FeCl_3$.

The effect of solvents was further extended to examine the loading of LiOH and formation of LiF in P1330 reverse micelles formed in toluene and o-xylene. We can discuss the loading of LiOH and connect this loading to the regions discussed in **Chapter 5.3.2**. The loading ratio used for LiOH was 1.19, which would place LiOH squarely in *Region III*, as outlined in **Chapter 5.3.2.2**.

However, if we analyze the topography of the LiOH loaded reverse micelles in toluene and o-xylene (**Figure 6.4**) we can see that loaded micelles can be clearly delineated. The ability to distinguish the loaded micelles despite their high loading ratio indicates that the LiOH loading seemingly falls in *Region II* where the relative Young's modulus and nanoparticle size have not reached an effective maximum. Furthermore, we can potentially explain the differences in loading ratio as a result of different interaction mechanisms. In the case of the $FeCl_3$ loading, we noted direct interactions between the $FeCl_3$ and P2VP block. However, this is not the case for LiOH. There is no evidence of LiOH interactions with the P2VP in either FTIR or RAMAN analysis, leading to our hypothesis that this method is primarily driven by osmosis.[65] It is likely that the difference in loading ratios is most likely due to the differences in interaction
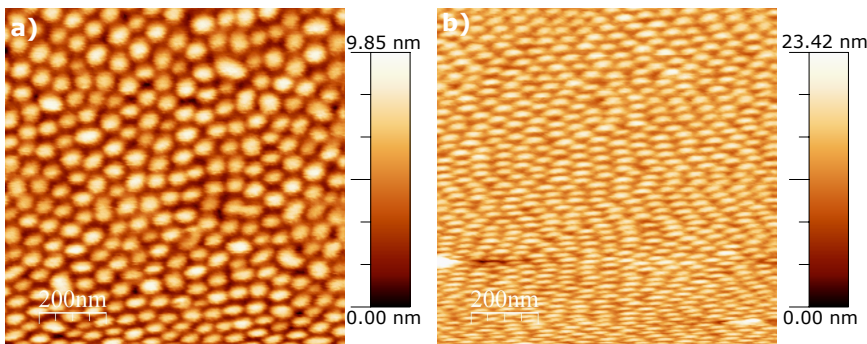
Figure 6.4: AFM topography of the LiOH loaded P1330 micelles in toluene (**a)**) and o-xylene (**b)**). Individual micelles are still evident, indicating the loaded LiOH amount is within *Region II*.

mechanism. It seems a higher molar ratio is needed to infiltrate when no interaction is occurring between the salt and P2VP.

We can further confirm that the LiOH loaded micelles fall within *Region II* by analyzing the Gaussian distribution of the Young's modulus for the loaded micelles. In the loaded LiOH cases, the Gaussian still exhibits a relatively narrow distribution. We know that as the loading ratio enters *Region III*, the Gaussian becomes wider, indicating that this particular loading of LiOH falls within *Region II*.

Figure 6.5 shows the relative Young's modulus for the P1330 micelles loaded with LiOH and LiF in toluene and o-xylene. Similar to **Chapter 5.3.2**, we notice an increase in the relative Young's modulus after loading. However, as previously discussed the interaction mechanism is different in the case of the LiOH. In the LiOH loading, we are measuring a three part composite of PS, P2VP, and LiOH through the centre of the micelle. This differs from the $FeCl_3$ where we are only measuring a two part system, PS and P2VP complexed with $FeCl_3$.

Figure 6.5 also shows that the o-xylene continues to be relatively stiffer than the toluene when the LiOH precursors are loaded into the micelle. The relative increase continues to hold when the LiF nanoparticles are formed in the micelle. The increase from LiOH to LiF is approximately 1.2 in both the toluene and o-xylene which we believe is a result of intrinsic differences between the hardness of the LiOH and LiF. Literature shows that the hardness value for LiOH and LiF are approximately 50 GPa and 70 GPa respectively, confirming that their should be an increase in the relative Young's modulus once the LiF is formed.[66]

However, the staircase effect noted in **Figure 6.5** does not seem to be explained
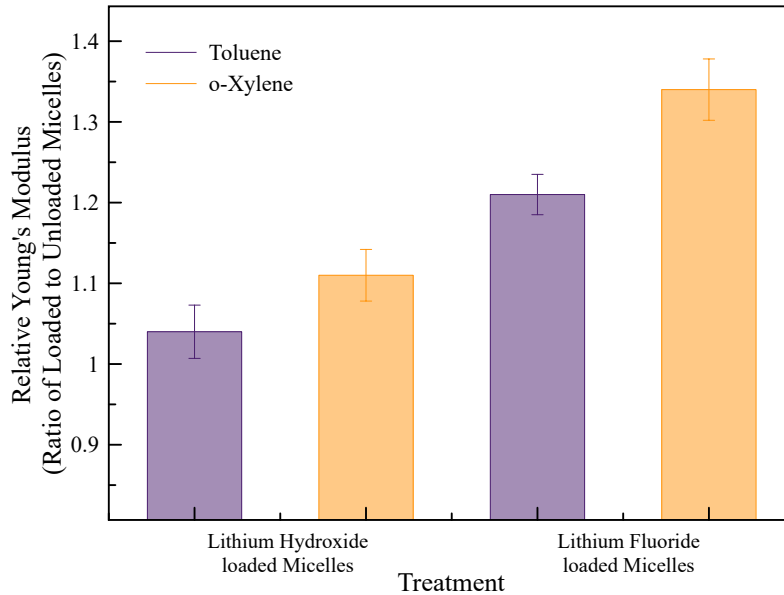
Figure 6.5:   Relative Young's modulus results show that the increase in Young's modulus as a result of salt loading and nanoparticle formation is more extreme in the case of the o-xylene micelles.

solely by differences between the solvents. If the solvent effect was the sole cause for the differences in raw Young's modulus values, we would expect the analysis of the relative Young's modulus to show the same value as in the case of o-xylene, the stiffer loaded films are being normalized by a stiffer unloaded film which should remove the influence of the solvent. We believe further variations in the relative Young's modulus can be related back to the resultant nanoparticle films.

6.3.4   Effects on Nanoparticles

To further explain the differences noted in **Figure 6.5**, we analyzed the size and dispersion of the resultant nanoparticle arrays. We noted a difference in the size and polydispersity of the nanoparticles which relates to the solvent used. The toluene nanoparticles had a size of 16.95 ± 3.29 nm and a PDI of 0.19. The o-xylene nanoparticles had a size 13.84 ± 1.78 nm and a PDI of 0.13. We can see here that the o-xylene makes smaller nanoparticles with less variations in size.

We also applied our in house tools to analyze the nanoparticle arrays displayed in the topography AFM images. The result of the array analysis are presented in

Figure 6.6. The inset of **Figure 6.6 (a) and (b)** show an order cloud for the nearest neighbour of the nanoparticle arrays. The o-xylene inset shows that o-xylene array exhibits a distinctly hexagonal packing with nanoparticles having six nearest neighbours. **Figure 6.6 (c) and (d)** show the pair correlation function for the toluene and o-xylene arrays. The o-xylene PCF (**Figure 6.6 (d)** shows a distinct peak for the nearest neighbour and the resultant PCF more closely resembles the PCF of a hexagonal lattice. The PCF of the o-xylene clearly shows the nanoparticle array is more ordered than the toluene array. Additionally lattice disorder parameters were extracted for the toluene and o-xylene micelles as 9.03 and 0.88 respectively, further indicating that the o-xylene produces a more ordered nanoparticle array.

Lastly, **Figure 6.6 (e) and (f)** shows the voronoi cells of the topography images. The grey cells represent particles with six nearest neighbours. In this case the o-xylene image has more grey cells which classifies it as more hexagonally packed than the toluene.

Given the differences noted in the size and order of the nanoparticle arrays, we reconnected these results to studies of the hardness of composite nanoparticle and polymer films and micelles.

We found that the increase in the relative Young's modulus for the o-xylene could be explained as a function of the resultant nanoparticle films. The literature has shown that the Young's modulus of polystyrene nanospheres coated in a metal shell increases when the size of the polstyrene sphere and the thickness of the metal shell increase.[67, 68] Of particular interest for our analysis is the relationship between the Young's modulus and size if the polystyrene nanospheres where the Young's modulus increases for an increasing polystyrene nanosphere with a constant metal shell thickness. This study indicates that as the relative amount of metal to the amount of PS decreases, the Young's modulus increases.[68] We see a similar relationship when we look at the size of the resultant nanoparticles relative to the size of the corona. In the case of toluene the resultant nanoparticles are approximately the same size as the corona, where as the nanoparticles in o-xylene are much smaller than the corona. The relative nanoparticle content to the thickness of the polystrene has decreased for the o-xylene leading to an increased modulus.

Further, the polydispersity of nanoparticles has been linked to the Young's modulus of a ligated nanoparticle film.[69] An anlaysis of multiple ligated nanoparticle films of the same nanoparticle size but different polydispersities showed that a higher polydispersity
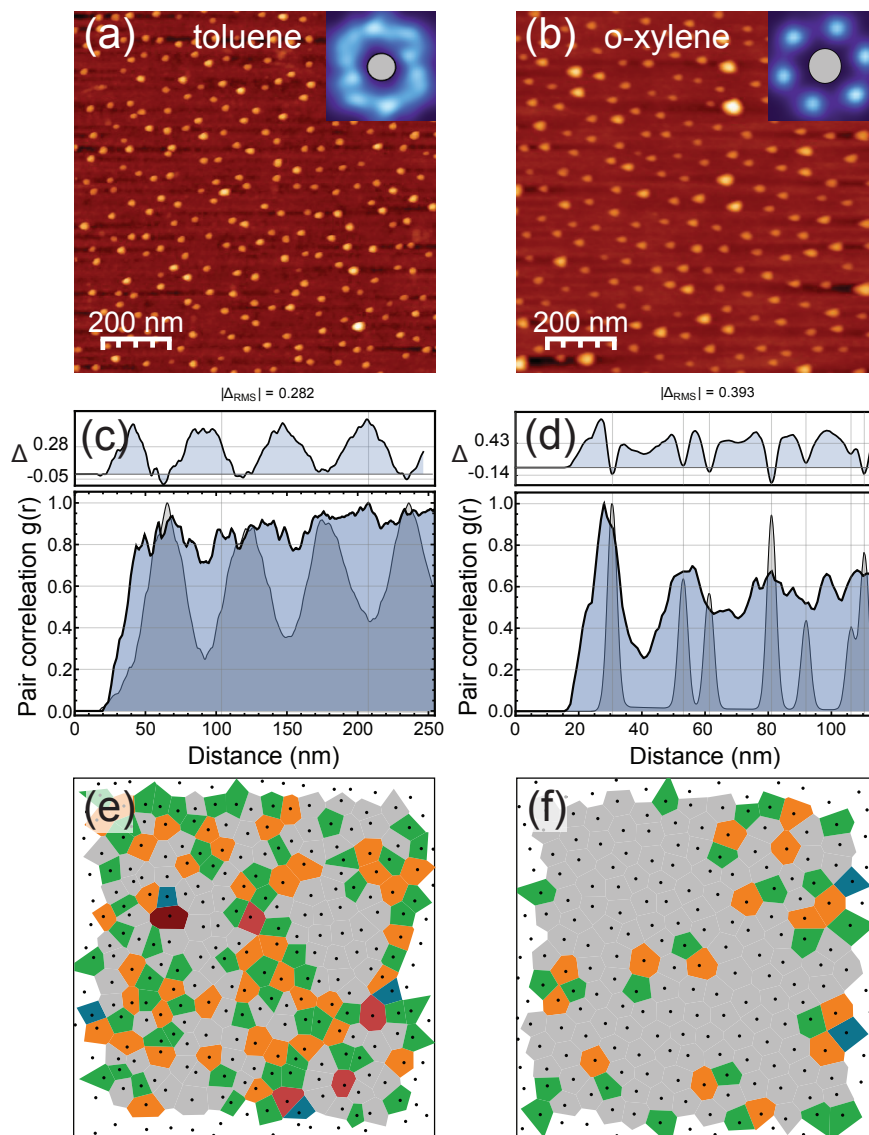
Figure 6.6: AFM images of the resultant lithium fluoride nanoparticle film for toluene (a) and o-xylene (b). The dispersion analysis indicates that the resultant nanoparticle array is more ordered using the o-xylene solvent.

decreases the Young's modulus of the film.[69] The resultant toluene nanoparticles had a greater polydispersity than the o-xylene nanoparticles. The difference between the Young's modulus of the loaded micelles can therefore be described as a result of the increased polydispersity and perceived inconsistent loading of the toluene reverse micelles.

6.4   Conclusion

Overall, the solvent studies show that the solvent can be used to tune the nanoparticle array and micelle system. Solvents can make it more difficult more salts to infiltrate the reverse micelle leading to smaller nanoparticles. More studies should be done to see if these effects can be extended to other solvents and reverse micelle co-polymers.

Chapter 7

Universality of the Loading Curve

7.1 Introduction

Based on the successful application of the QNM measurement methods to the $FeCl_3$ and LiF systems, we were interested in quantifying the universality of these methods.

A wide range of materials are commonly created using the reverse micelle nanoreactor technique. We wanted to test the universality of our approach and the resultant relative Young's modulus and loading ratio curves.

7.2 Experimental Methods

All experiments followed a similar reverse micelle loading protocol to those listed in **Chapters 5 and 6**. The tests were extended to indium acetate, zinc acetate, tin chloride, and methylammonium iodide salts.

7.2.1 Indium Acetate

Loaded solutions were prepared by dissolving 15 mg of the P1330 PS-*b*-P2VP copolymer in 5 mL of toluene. The solutions were stirred for 24 hours at room temperature to form reverse micelles. After 24 hours, indium acetate (Sigma Aldrich) was added to the reverse micelles solutions to create solutions with a loading ratio of 0.20, 0.39, 0.59, and 1.20. The loading ratio was determined based on the molar ratio of indium acetate to the P2VP block of the reverse micelle copolymer. Solutions were stirred for

an additional 24 hours at room temperature proceeding the salt addition to allow for the salts to infiltrate the core of the reverse micelles.

7.2.2   Zinc Acetate

Loaded solutions were prepared by dissolving 15 mg of the P1330 PS-*b*-P2VP co-polymer in 5 mL of toluene. The solutions were stirred for 24 hours at room temperature to form reverse micelles. After 24 hours, zinc acetate (Sigma Aldrich) was added to the reverse micelles solutions to create solutions with a loading ratio of 0.24, 0.41, 0.61, and 1.20. The loading ratio was determined based on the molar ratio of zinc acetate to the P2VP block of the reverse micelle copolymer. Solutions were stirred for an additional 24 hours at room temperature proceeding the salt addition to allow for the salts to infiltrate the core of the reverse micelles.

7.2.3   Tin Chloride

Loaded solutions were prepared by dissolving 15 mg of the P1330 and PS-*b*-P2VP co-polymer in 5 mL of toluene 15 mg of the P4824 and PS-*b*-P2VP co-polymer in 5 mL of toluene. The solutions were stirred for 24 hours at room temperature to form reverse micelles. After 24 hours, tin chloride (Sigma Aldrich) was added to the reverse micelles solutions to create solutions with a loading ratio of 0.11, 0.22, 0.33, 0.55, 0.66 and 0.99 in P1330 a loading ratio of 0.11, 0.33, 0.55, 0.66, 0.99 and 1.55. The loading ratio was determined based on the molar ratio of zinc acetate to the P2VP block of the reverse micelle copolymer. Solutions were stirred for an additional 48 hours at room temperature proceeding the salt addition to allow for the salts to infiltrate the core of the reverse micelles. After 48 hours, 0.3 mL of ethanol was added to react with the tin chloride to form tin oxide. Solutions were stirred for an additional 48 hours at room temperature proceeding the addition of ethanol to allow the tin oxide to form.

7.2.4   Methylammonium Iodide

Loaded solutions were prepared by dissolving 15 mg of the P1330 PS-*b*-P2VP co-polymer in 5 mL of o-xylene. The solutions were stirred for 24 hours at room temperature to form reverse micelles. After 24 hours, methylammonium iodide (MAI) (Greatcell Solar Ltd.) was added to the reverse micelles solutions to create solutions

with a loading ratio of 0.2. The loading ratio was determined based on the molar ratio of MAI to the P2VP block of the reverse micelle copolymer. Samples were taken time intervals of 6, 12, 18, 24, and 32 hours after salt addition to determine the amount of precursor salt infiltrated.

7.3   Results

7.3.1   Acetate Loading

In order to determine the universality of our approach, we began with a comparison of the indium acetate system to the iron chloride system. Indium acetate was selected due to its tendency to interact with P2VP[5] and in-house use for formation of ITO nanoparticles.

A summary of the iron chloride system is noted in **Figure7.1 (a)**. In the iron chloride system, we had defined *Region I* as having a loading ratio between 0 and 0.15, with predominate interactions occurring between the low level of salts and the PS region of the micelle. In this region, the interactions in the corona of the micelle produced a micelle with a lower Young's modulus than the unloaded micelle, resulting in a relative Young's modulus of less than one. *Region II* was defined as having a loading ratio between 0.15 and 0.4, where interactions are predominately between the salt and P2VP at the centre of the micelle. In this region, the Young's modulus was found to increase with the amount of salt loaded and resultant nanoparticle size. Finally, *Region III* was defined as having a loading ratio of greater than 0.4 where continued addition of the salt results in the eventual destruction of the micelle due to increased interactions along the P2VP backbone. In this region, the Young's modulus appears to plateau and the resultant nanoparticle arrays have a measured poor order.

Using these definitions for the different regions, we examined indium acetate loading and looked for similarities. The first feature noted was an extension of the *Region I* zone. For indium acetate, this loading region extends to just under 0.4 as loading ratios up to 0.39 exhibited a relative Young's modulus of less than one.

In this case, it was difficult to quantify the end of *Region II* and *Region III.* In the iron chlroide case, we used the order of the nanoparticle array to determine the end of *Region II* in addition to our ability to delineate whole micelles in the Young's modulus map. The indium acetate used here was an intermediate step for the creation of ITO

nanoparticles. As such, we have no information related to the nanoparticle arrays of indium acetate. After looking at **Figure 7.2**, we can observe very few differences between the low loaded and highligh loaded indium acetate micelles. Majority of the loaded micelles can still be delineated, indicating that this high loading may belong in *Region II*. However, as noted in **Figure 7.1 (b)**, it seems the micelle almost immediately approaches a maximum relative Young's modulus upon exiting *Region I*. There seems to be very little difference between the relative Young's modulus of the 0.59 and 1.2 loading ratios. Given the small difference in the relative Young's modulus we believed the end of *Region II* to be around 0.7.

We can see from the comparison between the iron chloride and indium acetate systems, that the values, region size, and *Region III* behaviour are not constant between salts. However, these results seem to indicate a universality for the loading regions, whereby each salt exhibits three distinct loading regions.

We further extended our analysis of relatively strong interacting salts by testing zinc acetate. Zinc acetate is also know to complex with P2VP.[4] We performed a study on zinc acetate used as an intermediate for zinc oxide formation. The results are noted in **Figure 7.1 (c)** show that the minimum loading used here was did not result in a film with a relative Young's modulus less than 1. Here, it appears that we have a larger *Region II* than the iron chloride and indium acetate cases. The separation between *Region II* and *Region III* was again challenging to separate as the zinc acetate was used as an intermediate step for zinc oxide formation and we are not able to directly calculate the zinc acetate nanoparticle size. Given the gap in relative Young's modulus between the 0.61 and 1.2 loadings is less than the 0.41 and 0.61 loading, we felt the cut off would be close to the 0.61 loading.

Additionally, the zinc acetate showed no indication of a *Region I* in the loading amounts used. As we did not test loading ratios lower than 0.24, we could not confirm the existence of a *Region I*.
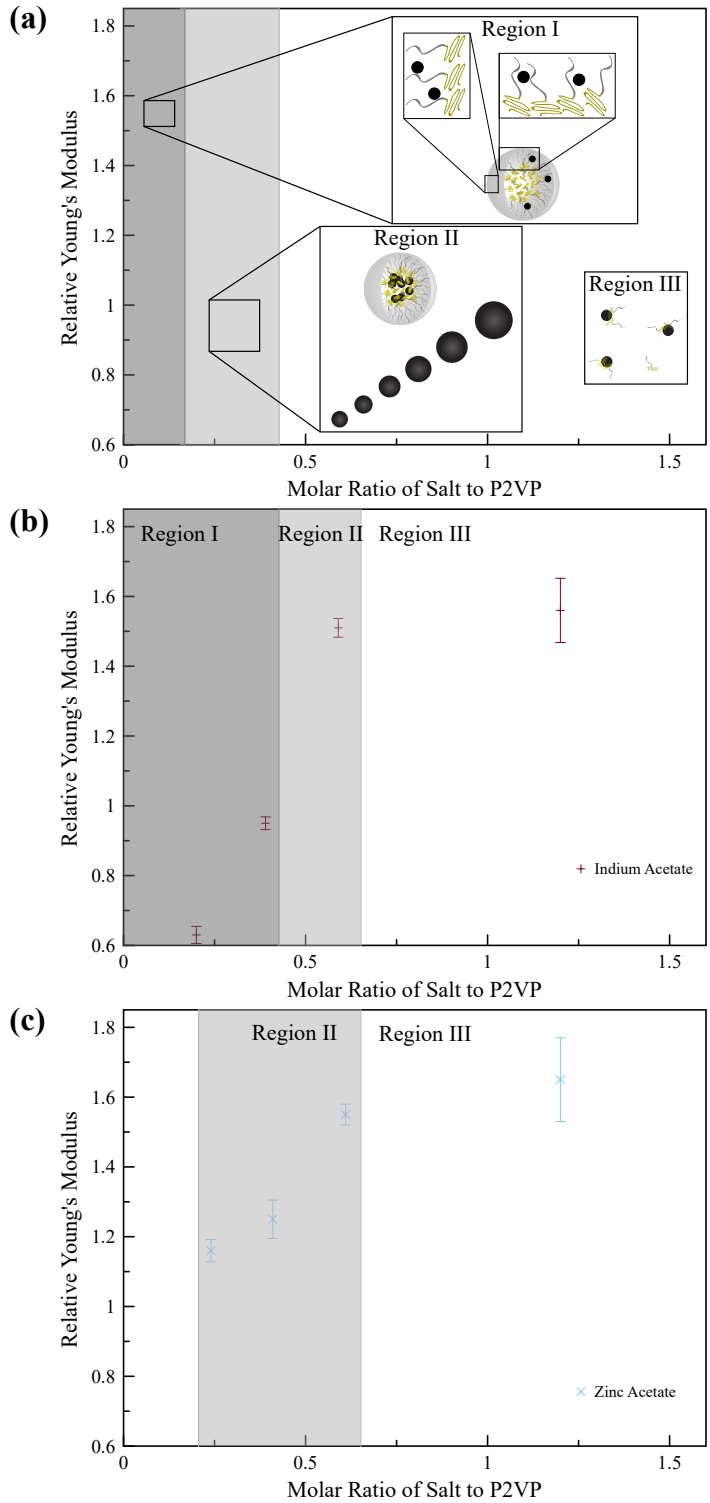
Figure 7.1: The loading regimes noted in the FeCl$_3$ [(a)] were used as a starting point to compare the loading of other salts. Indium acetate [(b)] showed a much larger *Region I*, and a smaller *Region II* compared to the FeCl$_3$. The loadings used for zinc acetate showed no indication of a *Region I*, but a larger *Region II*.
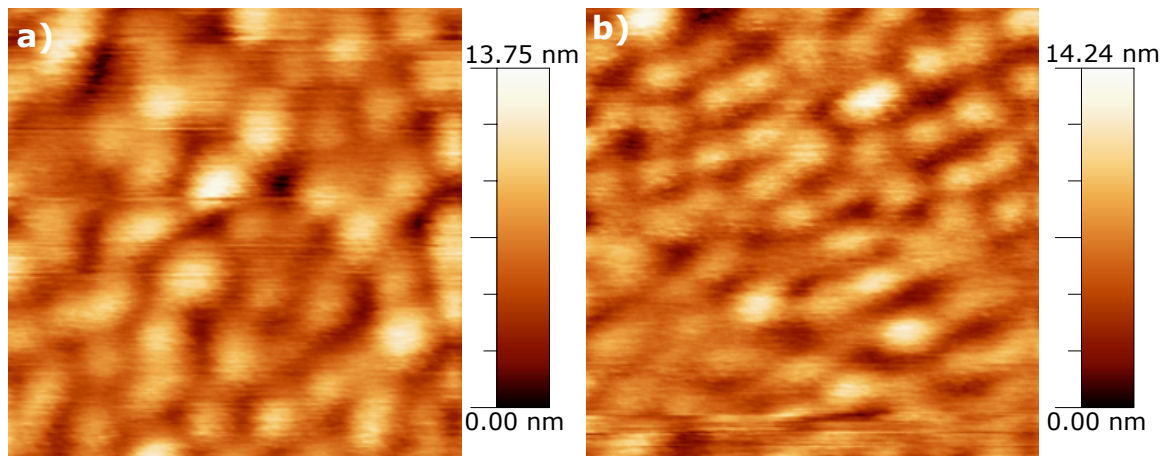
Figure 7.2: AFM images of micelles with low loading (a) and high loading (b) of indium acetate. Micelles still appear to be intact at high indium acetate loadings.

7.3.2   Tin Chloride Loading

A comprehensive analysis of a two-step loading process was preformed for a tin oxide system, made by the direct loading of tin chloride followed by the addition of ethanol after 24 hours loading time. We were interested to see if trends still existed after the formation of nanoparticles. We also used this test to see if any differences could be noted between the P1330 and P4824 polymers. Unike iron chloride, tin chloride does not show a P2VP complex on FTIR or RAMAN but a P2VP-tin complex is hypothesized.[5]

The previously discussed regions were applied to the tin chloride loadings and can be seen in **Figure 7.3 a)**. There are occasional difference between the P1330 and P4824 measurements, however they seem to fall within error of each other indicating no significant difference between co-polymers for the loading of tin chloride.

Region I was again determined as having a loading ratio less than one. In this case, we extended the loading limit to just past 0.2 as the 0.22 loading ratio for P1330 had a value of one, which we believe indicated that interaction were still predominately in the corona and had not yet reached the centre.

A combination of the nanoparticle heights, nanoparticle array parameters (both presented in **Tables 7.1 and 7.2**) and the loaded micelle images (presented in **Figure 7.4**) led us to believe that no *Region III* exists for the loading ratios used in this system. The nanoparticle height continues to increase with the loading ratio while the PDI of the nanoparticles shows small fluctuations. The loaded micelle images show

Table 7.1: Summary of nanoparticle height and polydispersity index for resultant SnO nanoparticles made with P1330.

Loading Ratio	Average Height (nm) ± SD	PDI	Nearest Neighbour Distance (nm)	Lattice Disorder Parameter
0.11	7.7 ± 1.2	0.2	45.6	12.6
0.22	10.4 ± 1.8	0.2	35.2	32.0
0.33	12.8 ± 2.9	0.2	44.7	21.9
0.55	15.6 ± 1.7	0.1	41.1	20.9
0.66	20.1 ± 3.8	0.2	35.8	17.5
0.99	21.5 ± 2.1	0.1	38.7	30.1

Table 7.2: Summary of nanoparticle height and polydispersity index for resultant SnO nanoparticles made with P4824.

Loading Ratio	Average Height (nm) ± SD	PDI	Nearest Neighbour Distance (nm)	Lattice Disorder Parameter
0.11	4.8 ± 0.7	0.1	47.8	12.6
0.33	9.7 ± 1.9	0.2	36.5	32.0
0.55	14.9 ± 1.4	0.1	36.7	21.9
0.66	17.6 ± 2.2	0.1	25.1	20.9
0.99	20.8 ± 3.2	0.1	35.8	17.5
1.55	26.4 ± 3.7	0.1	32.5	30.1

no an increase in swelling of the micelle, but there is no complete destruction of the micelles as experienced during the iron chloride loading. These results indicate a more drawn out *Region II* for the tin chloride loading. Further analysis of extreme loadings should be done to quantify the end of *Region II* and the universality of the *Region III*

After addition of tin chloride, the ethanol was added to form tin oxide within the micelles. The relative Young's modulus of the loaded micelle were analyzed to check if the regions have shifted after the formation of a nanoparticle within the micelle core. Results for this analysis are presented in **Figure 7.3 b)** Literature has indicated that increases in nanoparticle size (and by extension weight concentration) can result in a stiffer nanoparticle-polymer composite film.[70]

We can apply these studies by considering the loaded micelle as a three part composite film, where the nanoparticle is sandwiched between two layers of co-polymers.

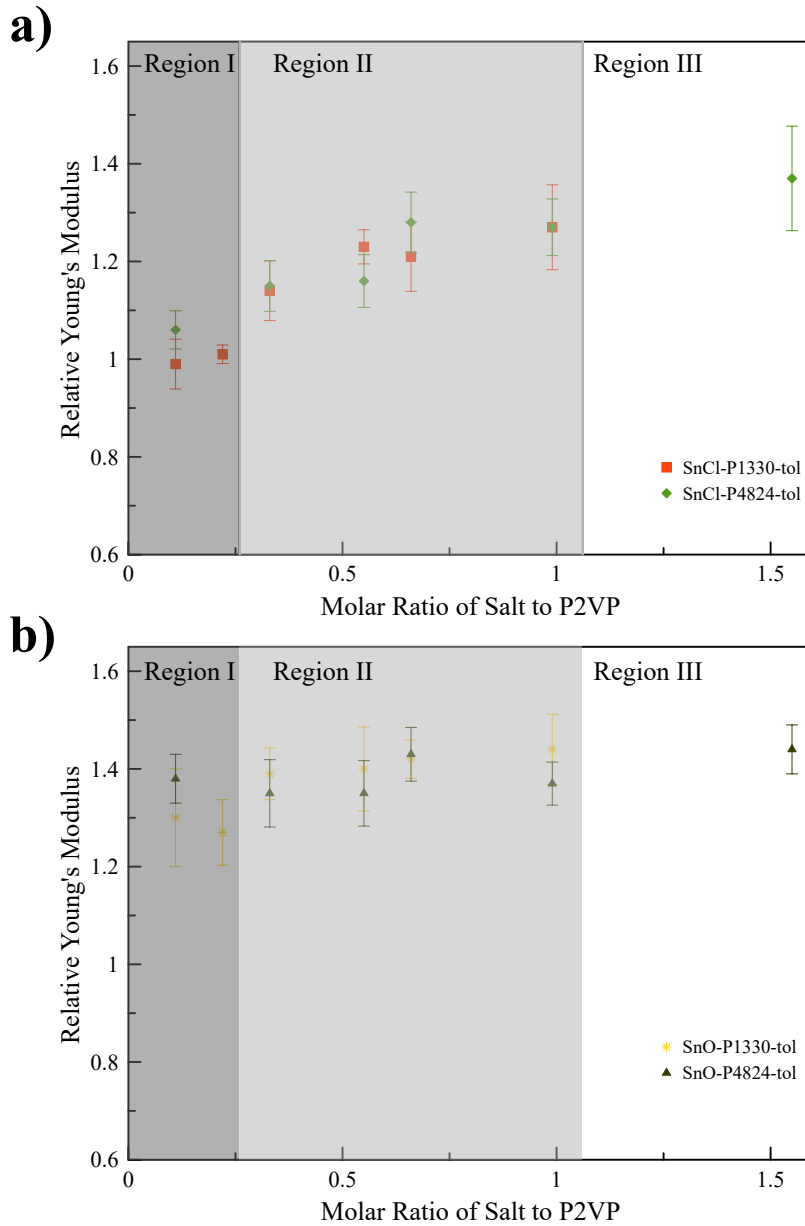Figure 7.3: Relative Young's modulus plotted against the molar ratio for tin chloride loading showed a similar regions noted in the iron chloride (a). Some minor differences were noted between polymers, but measurements generally fell within each other. After the addition of ethanol, tin oxide nanoparticles were formed and the relative Young's modulus appeared constant regardless of loading amount.
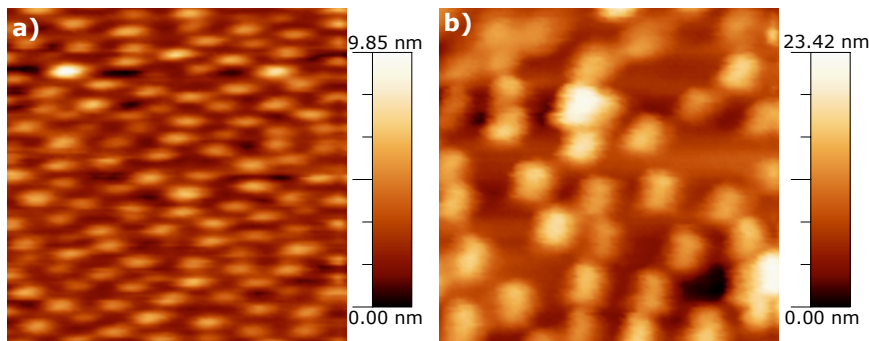
Figure 7.4: AFM images of micelles with low loading (a) and high loading (b) of tin chloride.

An analysis using the smallest nanoparticle size for P1330 and the corona thickness values from the empty micelle chapter showed an estimated relative Young's modulus of approximately 3. The analysis indicated that for the thickness of the P1330 corona, a nanoparticle size of 1.1 nm would result in the relative Young's modulus we measured. Additionally, we would expect the results presented in **Figure 7.3 b)** to correlate with the nanoparticle size, however what we see is a mix of relative Young's modulus values at approximately 1.4, regardless of their prior regionality.

Based on our observations, we believe the relative Young's modulus is dominated by the Young's modulus of the nanoparticle for fully formed nanoparticles. Once the nanoparticle precursor salts have reacted to form the nanoparticle, there should no longer be complexation in the P2VP block. We could then consider our QNM measurements to be of a polymer brush film sitting on top of the nanoparticle. During our measurements, the calibration process is against a silicon substrate. In the case of the the fully formed nanoparticles, the measured 1.4 value could be a result of the difference in Young's modulus between silicon and a tin oxide nanoparticle array on silicon.

The variations around 1.4 would be explained by the differences in PDI of the nanoparticle film. As discussed in **Chapter 6.3.4**, nanoparticle arrays with lower PDIs have been shown to exhibit a higher relative Young's modulus. **Tables 7.1 and 7.2** indicate that the P4824 nanoparticles have a smaller PDI. **Figure 7.3 b)** shows that typically the P4824 films have a higher relative Young's modulus, further confirming this finding.

Ultimately, it is unclear why the relative Young's modulus is stagnate at approximately 1.4 for the reverse micelles loaded with completely formed tin oxide. Additional

analysis of our system is needed to fully understand the reasoning behind the values measured for the formed nanoparticles.

7.3.3   Perovskite Loading

Further analysis of the universality led to the investigation of infiltration times. Our typical procedure was to allow salts to infiltrate the micelle core for 24 hours. We were curious to see if changing the time would result in a curve similar to the loading ratio curve, as we believed decreasing the infiltration time would result decrease the amount of salt infiltrated.

The analysis presented in **Figure 7.5** showed our hypothesis was correct. The Young's modulus maps and line profiles show the micelle core becomes stiffer as the methlyammonium iodide (MAI) salt is allowed to infiltrate for longer.

The relative Young's modulus graph presented in **Figure 7.5 (g)** is similar to the graphs previously discussed. For this set loading ratio of MAI, there appears to be no *Region I.* However, the analysis of a lower infiltration time may show the existence of a time-based *Region I.* Majority of the points collected align with the previously discussed definition of *Region II.* It seems that the longer the solution is allowed to infiltrate, the stiffer the micelle core becomes, indicating an increase in the amount of salt infiltrated.

However, the infiltration appears to come to a maximum just after 24 hours. The data point collected at 32 hours has slightly increased but falls within error of the 24 hour data point. This seemed to indicate the maximum loading time was 24 hours, though further data points of larger infiltration times may be needed to confirm this finding.

This study further confirmed the existence of a second *Region III* mode. As discussed earlier, for some salts the micelles are not destroyed at the maximum loading in *Region III.* We noted that this destruction does not occur for MAI salts when the infiltration time is varied. The completely loaded micelle is stable in this case and additional loading does not infiltrate the micelle core or lead to destabilization.
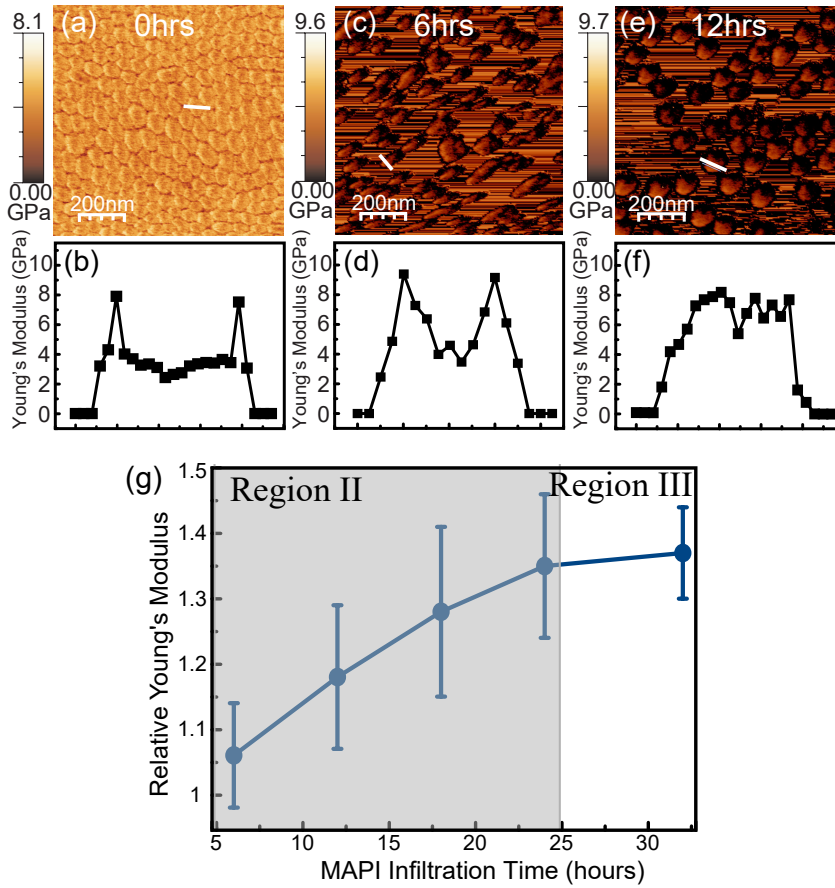
Figure 7.5: Young's modulus maps and line profiles for unloaded micelles [(a) and (b)] and methylammonium iodide (MAI) loaded micelles that have been allowed to infiltrate for 6 hours [(c) and (d)] and 12 hours [(e) and (f)]. The resultant relative Young's modulus graph (g) shows a gradual levelling out the the relative Young's modulus for increasing infiltration time.

7.4   Discussion

Based on our examination of additional loading systems, it seems evident that the different regions are universal for each systems but the exact loading ratios, relative Young's modulus values of *Region II* and *Region III*, and behaviour in *Region III* are dependent on the salt.

Figure 7.6 shows a summary of the interaction modes for each universal region. **Figure 7.6 (a)** shows that in *Region I* the primary mode of interaction is the intercalation of small amounts of loaded salts in the PS region of the micelle corona. This is the only region where the relative Young's modulus values are consistent across all salts at a value of less than one.

As salt amounts increase, the loading progresses to *Region II* as represented by **Figure 7.6 (b)**. In *Region II* the primary mode of interaction is dependent on the strength of the salt-P2VP interaction. Typically, reactive salts will complex with the P2VP block of the co-polymer, whereas infiltration of non-reactive salts is governed by osmosis. In both cases, the loaded salt will be localized to the micelle core. In this region, the increasing the salt leads to a larger relative Young's modulus and large resultant nanoparticles.

Lastly, further additions of salt pushes the systems into *Region III*, as typified by **Figure 7.6 (c)**. In this regions there are two proposed modes dependent of the interaction strength between P2VP and the loaded salt. **Figure 7.6 (c) i.** shows the mode for strong interacting salts. These salts will complex along the backbone of the P2VP and will destabilize the micelles in extreme excess loading scenarios, destroying the reverse micelle film. **Figure 7.6 (c) ii.** shows the mode for weak interacting salts. These salts are pushed into the micelle core through osmosis. The weak interaction will have no effect of the micelle structure, but salts will no longer be able to infiltrate. In both modes, the start of *Region III* is typified by the plateau of the relative Young's modulus where addition of further salts leads to smaller increases in the relative Young's modulus, if any at all. For strong interacting salts, this region can be seen by the destruction of the reverse micelle film.
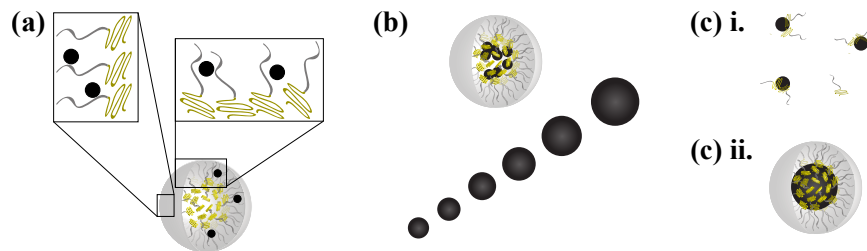
Figure 7.6:   Analysis indicates that regardless of salt type, three regions tend to appear in the relative Young's modulus graph. *Region I* (a) is where small amounts of salt infiltrate primarily in the PS region. *Region II* (b) is where salt infiltrates into the centre of the micelle, leading to a larger relative Young's modulus and resultant particle size. *Region III* has two proposed mechanisms. In case where the salt-P2VP interaction is strong, the micelles are destroyed [(c) i.]. In cases of a weak salt-P2VP interaction, the micelles fill to a maximum and the relative Young's modulus levels out.

Chapter 8

Conclusion

Chapter 4 explores the properties of the unloaded reverse micelles. The QNM-AFM results here showed a decrease in the Young's modulus of the reverse micelle through the centroid of the micelle. This decrease was consistent for all three co-polymers used. Three models were used to describe the decrease in Young's modulus across the centroid as a result of the intrinsic difference between the co-polymer blocks, as a result of the thin-shelled empty sphere created by dissolving the co-polymer in a selective solvent, and as a result of the micelle acting as a polymer brush when the AFM tip interacts with the centroid of the micelle. The end result indicated a combination of the intrinsic difference and polymer brush model best described the changes in nanomechanical properties across the micelle.

Chapter 5 explores the loading of the reverse micelle with iron chloride. The QNM-AFM results here show a three region trend where the relative Young's modulus changes with the molar ratio of additional salt. *Region I* is where small amounts of added salt intercalate with the PS block of the reverse micelle, leading to a slight decrease in the relative Young's modulus. *Region II* is where increasing the amount of loaded precursor salt leads to increase in the Young's modulus and size of the resultant nanoparticle. *Region III* is where further increase in the amount of loaded precursor salt leads to little to no further increases in the relative Young's modulus and nanoparticle size as well as a decrease in the order of the resultant nanoparticle film and destruction of the reverse micelles. For the iron chloride, it appears the interaction mechanism is the complexation of the iron chloride with the P2VP.

Chapter 6 explores the effect of solvents on the unloaded micelles and the loading

of precursors. This QNM-AFM results note that o-xylene results in slightly stiffer micelles with a larger micelle diameter and corona size than the toluene. The stiffness increase extended to the loaded micelle, an interesting phenomenon as the o-xylene micelles produced a smaller particle. The relative Young's modulus was linked back to the PDI of the nanoparticles, as nanoparticles with a smaller PDI result in a greater increase in mechanical properties. The o-xylene micelles produced nanoparticles with a smaller PDI, verifying this relation.

Lastly, Chapter 7 explores the universality of the loading curve. In this chapter, we examined the loading of reverse micelles with indium acetate, zinc acetate, tin chloride, and methylammonium iodide. We were interested to see if the maximum relative Young's modulus, molar loading ratios and the trend seen in Chapter 5 would be consistent with multiple salts. Our results showed the trend to be the key universal factor of these study. All the salts examined had loading ratios that fell within most or all of the regions previously discussed. However, the value of the loading ratio and relative Young's modulus were not consistent. These results also proposed an additional *Region III*, where the maximum infiltration is reached but the micelles are still intact.

Reverse micelles are widely used as nanoreactors for the creation of nanoparticles. The results presented here are the starting point needed to gain an in-depth understanding of the mechanisms behind the loading of the reverse micelles and how these mechanisms may affect the size and dispersion of the resultant nanoparticle films.

Our results show a universal trend, where all precursor salts first decrease the relative Young's modulus with the addition of small amounts, followed by the linear increase of the nanoparticle size and the relative Young's modulus with the addition of further precursor salts. Finally, the relative Young's modulus will reach a where further addition of precursor salt leads to little or no change in the relative Young's modulus, indicating either the complete filling of the reverse micelle or their destruction.

Chapter 9

Future Work

This study presents the starting for a deeper understanding of the underlying mechanisms and interactions involved in the reverse micelle nanoreactor process. A great deal of work is required to gain a complete understanding of the reverse micelle nanorecator process.

Firstly, the results of **Chapter 4** should be extended to other PS-*b*-P2VP co-polymer weightings. A more systematic study whereby the co-polymer weightings are changed for on of the blocks and not the other could provide a more in depth understanding of the unloaded system. The results of **Chapter 6** could be incorporated into this study to further understand how the solvent effects the unloaded micelle.

Second, the work of **Chapter5** should be extended to include additional co-polymers and solvents. This was the most extensive loading regime studied in this work, by extending it to multiple polymers and solvents, the universality could be explored for more than just various loading salts. Extending the robust iron chloride loading to o-xylene would quantify the effects of a different solvent across the loading spectrum. Using the P1330 or P9861 co-polymers across the entire loading spectrum would also help to provide some insight into the effect of polymer block length on the loading curve. It is currently unclear as to how the regions would respond if the core block length is shortened.

Lastly, the results of **Chapter 6** and **Chpater 7** should be extended to confirm the universality of the three loading regions across multiple salts. Work should focus on extending the lithium hydroxide and lithium fluoride work to more than one loading ratio to confirm the existence of the multiple loading regions for this precursor salt.

Further non-polar solvents should be explored to confirm the existence of multiple loading regions across multiple solvents. Further loading ratios should be explored for the indium acetate and zinc acetate systems so as to confirm the existence and size of all three loading regions. A systematic study should also be done with additional co-polymers to examine the effects extreme changes in block length have on the loading regions and systems.

Bibliography

[1] Gerd Kästle, Hans Gerd Boyen, Frank Weigl, Gunther Lengl, Thomas Herzog, Paul Ziemann, Silke Riethmüller, Oliver Mayer, Christoph Hartmann, Joachim P. Spatz, Martin Möller, Masaki Ozawa, Florian Banhart, Michael G. Garnier, and Peter Oelhafen. "Micellar Nanoreactors - Preparation and Characterization of Hexagonally Ordered Arrays of Metallic Nanodots". In: *Advanced Functional Materials* 13.11 (2003), pp. 853–861. ISSN: 1616301X. DOI: `10.1002/adfm.200304332` (cit. on pp. 1, 3, 39).

[2] Huda Yusuf, Whan-gi Kim, Dong Hoon Lee, Marie Aloshyna, Alexandre G Brolo, and Matthew G Moffitt. "A Hierarchical Self-Assembly Route to Three-Dimensional Polymer - Quantum Dot Photonic Arrays". In: *Langmuir* 23.17 (2007), pp. 5251–5254. DOI: `10.1021/la7002904` (cit. on p. 1).

[3] Jennifer Lu, Dongning Yuan, Jie Liu, Weinan Leng, and Thomas E. Kopley. "Three Dimensional Single-Walled Carbon Nanotubes". In: *Nano Letters* 8.10 (2008), pp. 3325–3329. ISSN: 1530-6984. DOI: `10.1021/nl801744z`. URL: `http://pubs.acs.org/doi/abs/10.1021/nl801744z` (cit. on p. 1).

[4] Osman El-atwani, Taner Aytun, Omer Faruk Mutaf, Vesna Srot, Peter A Van Aken, and Cleva W Ow-yang. "Determining the Morphology of Polystyrene-block -poly (2-vinylpyridine) Micellar Reactors for ZnO Nanoparticle Synthesis". In: *Langmuir* 26.20 (2010), pp. 7431–7436. DOI: `10.1021/la904143f` (cit. on pp. 1, 74).

[5] Hyeonghwa Yu and Ayse Turak. "Nanoreactors or nanoscale stablizers : routes for solution processed indium tin oxide nanoparticles by reverse micelle". In: *Canadian Journal of Physics* 92 (2014). DOI: `10.1139/cjp-2013-0549` (cit. on pp. 1, 6, 73, 76).

[6]   Stephan Förster and Markus Antonietti. "Amphiphilic Block Copolymers in Structure- Controlled Nanomaterial Hybrids". In: *Advanced Materials* 10.3 (1998), pp. 195–217. ISSN: 0935-9648. DOI: 10.1002/(SICI)1521-4095(199802)10:3<195::AID-ADMA195>3.0.CO;2-V (cit. on pp. 3, 24, 39, 40).

[7]   Hanqiong Hu, Manesh Gopinadhan, and Chinedum O Osuji. "Directed self-assembly of block copolymers: a tutorial review of strategies for enabling nanotechnology with soft matter." In: *Soft matter* 10.22 (2014), pp. 3867–3889. ISSN: 1744-6848. DOI: 10.1039/c3sm52607k. URL: http://www.ncbi.nlm.nih.gov/pubmed/24740355 (cit. on pp. 3, 39).

[8]   Cian Cummins, Tandra Ghoshal, Justin D Holmes, and Michael A Morris. "Strategies for Inorganic Incorporation using Neat Block Copolymer Thin Films for Etch Mask Function and Nanotechnological Application". In: *Advanced Materials* (2016), pp. 5586–5618. ISSN: 15214095. DOI: 10.1002/adma.201503432 (cit. on pp. 3, 39).

[9]   Ulf Wiedwald, Luyang Han, Johannes Biskupek, Ute Kaiser, and Paul Ziemann. "Preparation and characterization of supported magnetic nanoparticles prepared by reverse micelles". In: *Beilstein Journal of Nanotechnology* 1.1 (2010), pp. 24–47. ISSN: 21904286. DOI: 10.3762/bjnano.1.5 (cit. on pp. 3, 39).

[10] Lifeng Zhang and Adi Eisenberg. "Multiple Morphologies of " Crew-Cut " Aggregates of Polystyrene-b-poly (acrylic acid) Block Copolymers Author (s): Lifeng Zhang and Adi Eisenberg Published by : American Association for the Advancement of Science Stable URL : http://www.jstor.org/stab". In: *Science* 268.5218 (1995), pp. 1728–1731 (cit. on pp. 4, 5, 22, 56, 58).

[11] Lifeng Zhang and Adi Eisenberg. "Multiple Morphologies and Characteristics of " Crew-Cut " Micelle-like Aggregates of Polystyrene- b -poly (acrylic acid) Diblock Copolymers in Aqueous Solutions". In: *Journal of the American Chemical Society* 118.24 (1996), pp. 3168–3181. DOI: 10.1021/ja953709s (cit. on pp. 4, 22, 24).

[12] Matthew Moffitt, Lynne McMahon, Valerie Pessel, and Adi Eisenberg. "Size Control of Nanoparticles in Semiconductor-Polymer Composites. 2. Control via Sizes of Spherical Ionic Microdomains in Styrene-Based Diblock Ionomers". In: *Chemistry of Materials* 7.6 (1995), pp. 1185–1192. ISSN: 15205002. DOI: 10.1021/cm00054a018 (cit. on pp. 5, 39).

[13] Matthew Moffitt and Adi Eisenberg. "Size Control of Nanoparticles in Semiconductor-Polymer Composites. 1. Control via Multiplet Aggregation Numbers in Styrene-Based Random Ionomers". In: *Chemistry of Materials* 7.6 (1995), pp. 1178–1184. ISSN: 15205002. DOI: 10.1021/cm00054a017 (cit. on pp. 5, 39).

[14] Joachim P Spatz, Stefan Mössmer, Christoph Hartmann, Martin Möller, Thomas Herzog, Michael Krieger, Hans Gerd Boyen, Paul Ziemann, and Bernd Kabius. "Ordered deposition of inorganic clusters from micellar block copolymer films". In: *Langmuir* 16.2 (2000), pp. 407–415. ISSN: 07437463. DOI: 10.1021/la990070n (cit. on pp. 5, 7, 39, 40).

[15] Theobald Lohmüller, Daniel Aydin, Marco Schwieder, Christoph Morhard, Ilia Louban, Claudia Pacholski, and Joachim P. Spatz. "Nanopatterning by block copolymer micelle nanolithography and bioinspired applications". In: *Biointerphases* 6.1 (2011), MR1–MR12. ISSN: 1934-8630. DOI: 10.1116/1.3536839. URL: http://avs.scitation.org/doi/10.1116/1.3536839 (cit. on pp. 5, 6, 39, 40).

[16] Sébastien Roland, Cé Guinto Gamys, Josué Grosrenaud, Stéphanie Boissé, Christian Pellerin, Robert E. Prud'Homme, and C Geraldine Bazuin. "Solvent Influence on Thickness, Composition, and Morphology Variation with Dip-Coating Rate in Supramolecular PS-b-P4VP Thin Films". In: *Macromolecules* 48.14 (2015), pp. 4823–4834. ISSN: 15205835. DOI: 10.1021/acs.macromol.5b00847 (cit. on pp. 5, 55).

[17] Ekaterina B Zhulina, Mireile Adam, Isaac Larue, Sergei S Sheiko, and Michael Rubinstein. "Diblock Copolymer Micelles in a Dilute Solution". In: *Macromolecules* 38 (2005), pp. 5330–5351 (cit. on pp. 5, 55).

[18] Paschalis Alexandridis and Richard J Spontak. "Solvent-regulated ordering in block copolymers". In: *Current Opinion in Colloid & Interface Science* 4 (1999), pp. 130–139 (cit. on pp. 5, 55).

[19] S Polym Lett, S J Polym Sci, and Polym Lett Ed. "Polymer Swelling . 5 . Correlation of Relative Swelling of Poly (styrene-co-divinylbenzene) with the Hildebrand Solubility Parameter of the Swelling Liquid". In: *Macromolecules* 19.5 (1986), pp. 1522–1525 (cit. on pp. 5, 55, 64).

[20] L. A. Errede. "Polymer Swelling , 13 : Correlation of Flory-Huggins Interaction Parameter , X , with Molecular Structure in Polystyrene-Liquid Systems". In: *Journal of Applied Polymer Science* 45 (1992) (cit. on pp. 5, 55, 64).

[21] Hubert Elbs and Georg Krausch. "Ellipsometric determination of Flory-Huggins interaction parameters in solution". In: *Polymer* 45 (2004), pp. 7935–7942. DOI: 10.1016/j.polymer.2004.09.021 (cit. on pp. 5, 55).

[22] Ryan D Bennett, Andrew C Miller, Naomi T Kohen, Paula T Hammond, Darrell J Irvine, and Robert E Cohen. "Strategies for controlling the planar arrangement of block copolymer micelles and inorganic nanoclusters". In: *Macromolecules* 38.26 (2005), pp. 10728–10735. ISSN: 00249297. DOI: 10.1021/ma0518555 (cit. on pp. 6, 39).

[23] Peng Liu and Jiandong Ding. "Fabrication of micro-Nano hybrid patterns on a solid surface". In: *Langmuir* 26.1 (2010), pp. 492–497. ISSN: 07437463. DOI: 10.1021/la9021504 (cit. on pp. 6, 39).

[24] Tandra Ghoshal, Matthew T. Shaw, Ciara T. Bolger, Justin D. Holmes, and Michael A. Morris. "A general method for controlled nanopatterning of oxide dots: a microphase separated block copolymer platform". In: *Journal of Materials Chemistry* 22.24 (2012), p. 12083. ISSN: 0959-9428. DOI: 10.1039/c2jm30468f. URL: http://xlink.rsc.org/?DOI=c2jm30468f (cit. on pp. 6, 39).

[25] Sang Hyun Yun, Byeong Hyeok Sohn, Jin Chul Jung, Wang Cheol Zin, Jin Kyu Lee, and Ohsung Song. "Tunable magnetic arrangement of iron oxide nanoparticles in situ synthesized on the solid substrate from diblock copolymer micelles". In: *Langmuir* 21.14 (2005), pp. 6548–6552. ISSN: 07437463. DOI: 10.1021/la050418g (cit. on pp. 6, 40).

[26] Lianchen Shan, Sathya Punniyakoti, Margriet J Van Bael, Kristiaan Temst, Marlies K Van Bael, Xiaoxing Ke, Sara Bals, Gustaaf Van Tendeloo, Marc D'Olieslaeger, Patrick Wagner, Ken Haenen, and Hans-Gerd Boyen. "Homopolymers as Nanocarriers for the Loading of Block Copolymer Micelles with Metal Salts: A Facile Way to Large-scale Ordered Arrays of Transition-metal Nanoparticles". In: *Journal of Materials Chemistry C* 2.4 (2014), pp. 701–707. ISSN: 2050-7526. DOI: 10.1039/c3tc31333f. URL: http://dx.doi.org/10.1039/C3TC31333F (cit. on pp. 6, 40, 43, 51).

[27]   Yoshio Sageshima, Atsushi Noro, and Yushu Matsushita. "Structural isomer effects on the morphology of block copolymer/metal salts hybrids". In: *Journal of Polymer Science, Part B: Polymer Physics* 52.5 (2014), pp. 377–386. ISSN: 08876266. DOI: 10.1002/polb.23421 (cit. on pp. 7, 40, 42, 46, 48, 50).

[28]   Alim Solmaz, Taner Aytun, Julia K. Deuschle, and Cleva W. Ow-Yang. "Nanoscale elastic modulus variation in loaded polymeric micelle reactors". In: *Langmuir* 28.28 (2012), pp. 10592–10596. ISSN: 07437463. DOI: 10.1021/la3017722 (cit. on pp. 7–9, 40, 41).

[29]   Taner Aytun, Omer Faruk Mutaf, Osman J El-Atwani, and Cleva W Ow-Yang. "Nanoscale composition mapping of segregation in micelles with tapping-mode atomic force microscopy". In: *Langmuir* 24.24 (2008), pp. 14183–14187. ISSN: 07437463. DOI: 10.1021/la802384x (cit. on pp. 7–9, 40, 41).

[30]   B J Briscoe, L Fiori, and E Pelillo. "Nano-indentation of polymeric surfaces". In: *Journal of Physics D: Applied Physics* 31.19 (1998), pp. 2395–2405. ISSN: 0022-3727. DOI: 10.1088/0022-3727/31/19/006. URL: http://stacks.iop.org/0022-3727/31/i=19/a=006?key=crossref.73536d6a03661860265957fce4d75df5%20http://iopscience.iop.org/article/10.1088/0022-3727/31/19/006/meta (cit. on pp. 7, 8, 40, 41).

[31]   T. J. Young, M. A. Monclus, T. L. Burnett, W. R. Broughton, S. L. Ogin, and P. A. Smith. "The use of the PeakForceTM quantitative nanomechanical mapping AFM-based method for high-resolution Young's modulus measurement of polymers". In: *Measurement Science and Technology* 22.12 (2011). ISSN: 09570233. DOI: 10.1088/0957-0233/22/12/125703. arXiv: arXiv:1011.1669v3 (cit. on pp. 7, 9–11, 22, 40, 41).

[32]   Maxim E. Dokukin and Igor Sokolov. "Quantitative mapping of the elastic modulus of soft materials with HarmoniX and PeakForce QNM AFM modes". In: *Langmuir* 28.46 (2012), pp. 16060–16071. ISSN: 07437463. DOI: 10.1021/la302706b (cit. on pp. 7, 9, 40, 41, 43).

[33]   Mark R. VanLandingham, John S. Villarrubia, William F. Guthrie, and Greg F. Meyers. "Nanoindentation of polymers: An overview". In: *Macromolecular Symposia* 167.August 2000 (2001), pp. 15–43. ISSN: 10221360. DOI: 10.1002/1521-3900(200103)167:1<15::AID-MASY15>3.0.CO;2-T. arXiv: 1011.1669 (cit. on pp. 7, 8, 41).

[34] B. Cappella and G. Dietler. "Force-distance curves by atomic force microscopy". In: *Surface Science Reports* 34.1-3 (1999), pp. 1–104. ISSN: 01675729. DOI: 10.1016/S0167-5729(99)00003-5. URL: http://linkinghub.elsevier.com/retrieve/pii/S0167572999000035 (cit. on pp. 9, 41).

[35] Meng Yu and Albena Ivanisevic. "Encapsulated cells: An atomic force microscopy study". In: *Biomaterials* 25.17 (2004), pp. 3655–3662. ISSN: 01429612. DOI: 10.1016/j.biomaterials.2003.10.061 (cit. on pp. 9, 41).

[36] Yves F. Dufrêne, David Martínez-Martín, Izhar Medalsy, David Alsteens, and Daniel J. Müller. "Multiparametric imaging of biological systems by force-distance curve-based AFM". In: *Nature Methods* 10.9 (2013), pp. 847–854. ISSN: 15487091. DOI: 10.1038/nmeth.2602. URL: http://dx.doi.org/10.1038/nmeth.2602 (cit. on pp. 9, 41).

[37] Jozef Adamcik, Cecile Lara, Ivan Usov, Jae Sun Jeong, Francesco S. Ruggeri, Giovanni Dietler, Hilal A. Lashuel, Ian W. Hamley, and Raffaele Mezzenga. "Measurement of intrinsic properties of amyloid fibrils by the peak force QNM method". In: *Nanoscale* 4.15 (2012), p. 4426. ISSN: 2040-3364. DOI: 10.1039/c2nr30768e. URL: http://xlink.rsc.org/?DOI=c2nr30768e (cit. on pp. 9, 41).

[38] B V Derjaguin, V M Muller, and Y U P Toporov. "Effect of contact deformation on the adhesion of particles." In: *Journal of colloid and interface science* 52.3 (1975), pp. 105–108. ISSN: 00219797. DOI: 10.1016/0021-9797(75)90018-1 (cit. on pp. 10, 11, 22).

[39] Matthew R. Libera and Ray F. Egerton. "Advances in the transmission electron microscopy of polymers". In: *Polymer Reviews* 50.3 (2010), pp. 321–339. ISSN: 15583724. DOI: 10.1080/15583724.2010.493256 (cit. on p. 20).

[40] Linda Sawyer, David T. Grubb, and Gregory F. Meyers. *Polymer Microscopy*. 3rd. New York: Springer Verlag, 2008 (cit. on p. 20).

[41] Stephan Reiling, Marcel Besnard, and Philippe A Bopp. "Theoretical Studies on the Pyridine - I 2 Charge-Transfer Complex . 1 . Ab-Initio Calculations on I 2 and Pyridine - I 2". In: *Journal of Physical Chemistry A* 5639.97 (1997), pp. 4409–4415. DOI: 10.1021/jp9700138 (cit. on p. 20).

[42]   Alan Boyde, Fergus A. Mccorkell, Graham K. Taylor, Richard J. Bomphrey, and Michael Doube. "Iodine vapor staining for atomic number contrast in backscattered electron and X-ray imaging". In: *Microscopy Research and Technique* 77.12 (2014), pp. 1044–1051. ISSN: 10970029. DOI: 10.1002/jemt.22435 (cit. on p. 20).

[43]   NJ Jeon, JH Noh, WS Yang, YC Kim, S Ryu, J Seo - Nature, and Undefined 2015. "Compositional engineering of perovskite materials for high-performance solar cells". In: *Nature* 517 (2015). URL: https://www.nature.com/articles/nature14133?page=27 (cit. on p. 20).

[44]   Seong Il Yoo, Byeong Hyeok Sohn, Wang Cheol Zin, Jin Chul Jung, and Cheolmin Park. "Mixtures of diblock copolymer micelles by different mixing protocols". In: *Macromolecules* 40.23 (2007), pp. 8323–8328. ISSN: 00249297. DOI: 10.1021/ma071534o (cit. on p. 20).

[45]   Arkadii Arinstein, Michael Burman, Oleg Gendelman, and Eyal Zussman. "Effect of supramolecular structure on polymer nanofibre elasticity". In: *Nature Nanotechnology* 2 (2007), pp. 59–62. DOI: 10.1038/nnano.2006.172 (cit. on p. 22).

[46]   Zhisheng Gao, Sunil K. Varshney, Stanislaus Wong, and Adi Eisenberg. "Block Copolymer "Crew-Cut" Micelles in Water". In: *Macromolecules* 27.26 (1994), pp. 7923–7927. DOI: 10.1021/ma00104a058 (cit. on p. 24).

[47]   Yoshiaki Takahashi, Nobuo Ochiai, Yushu Matshushita, and Ichiro Noda. *Viscoelastic Properties of Poly(2-vinylpyridine) in Bulk and Solution.* 1996. DOI: 10.1295/polymj.28.1065 (cit. on p. 26).

[48]   Lijuan Zhang, Maria D'Acunzi, Michael Kappl, Gunter K. Auernhammer, Doris Vollmer, Carlos M. Van Kats, and Alfons Van Blaaderen. "Hollow silica spheres: Synthesis and mechanical properties". In: *Langmuir* 25.5 (2009), pp. 2711–2717. ISSN: 07437463. DOI: 10.1021/la803546r (cit. on p. 28).

[49]   Xiaojun Ma, Xing Tang, Zongwei Wang, Qian Chen, Menglu Qian, Jie Meng, Yongjian Tang, Hao Shen, and Dangzhong Gao. "Determination of elastic modulus for hollow spherical shells via resonant ultrasound spectroscopy". In: *Fusion Engineering and Design* 117 (2017), pp. 74–78. ISSN: 0920-3796. DOI:

10.1016/j.fusengdes.2017.02.050. URL: http://dx.doi.org/10.1016/j.fusengdes.2017.02.050 (cit. on p. 28).

[50] Jonas Riest, Labrini Athanasopoulou, Sergei A Egorov, and Christos N Likos. "Elasticity of polymeric nanocolloidal particles". In: *Nature Publishing Group* (2015), pp. 1–12. DOI: 10.1038/srep15854. URL: http://dx.doi.org/10.1038/srep15854 (cit. on p. 28).

[51] Robert Shorter, John D Smith, Vincent A Coveney, and James J C Busfield. "Axial Compression of Hollow Elastic Spheres". In: *Journal of Mechanics of Materials and Structures* 5.5 (2010) (cit. on p. 28).

[52] D.S Hughes and J.L. Kelly. "Second-Order Elastic Deformations of Solids". In: *Physical Review* 92.5 (1953), pp. 1145–1150. ISSN: 0031-899X. DOI: 10.1103/PhysRev.92.1145 (cit. on p. 34).

[53] P. B. Bowden and R. J. Young. "Deformation mechanisms in crystalline polymers". In: *Journal of Material Science* 9 (1974), pp. 2034–2051 (cit. on p. 34).

[54] Kevin M Knowles and Philip R Howie. "The Directional Dependence of Elastic Stiffness and Compliance Shear Coefficients and Shear Moduli in Cubic Materials". In: *Journal of Elasticity* 120 (2015), pp. 87–108. ISSN: 0374-3535. DOI: 10.1007/s10659-014-9506-1. URL: http://dx.doi.org/10.1007/s10659-014-9506-1 (cit. on p. 34).

[55] D Julthongpiput, M. LeMieux, and V V Tsukruk. "Micromechanical properties of glassy and rubbery polymer brush layers as probed by atomic force microscopy". In: *Polymer* 44.16 (2003), pp. 4557–4562. ISSN: 00323861. DOI: 10.1016/S0032-3861(03)00404-X (cit. on p. 35).

[56] Xianghui Zhang, Ihsan Amin, Marin Steenackers, Ning Zhang, Tobias Pirzer, Thorsten Hugel, Rainer Jordan, and Armin Go. "Polymer Carpets". In: *Small* 10.15 (2010), pp. 1623–1630. DOI: 10.1002/smll.201000448 (cit. on p. 35).

[57] S T Milner and T A Witten. "Bending moduli of polymeric surfactant interfaces". In: *Journal of Physics France* 49.11 (1988), pp. 1951–1962 (cit. on p. 35).

[58] Shinpei Yamamoto, Muhammad Ejaz, Yoshinobu Tsujii, Takeshi Fukuda, Mutsuo Matsumoto, and Takeshi Fukuda. "Surface Interaction Forces of Well-Defined , High-Density Polymer Brushes Studied by Atomic Force Microscopy . 2 .

Effect of Graft Density". In: *Macromolecules* (2000), pp. 5602–5607. DOI: 10.1021/ma991733a (cit. on p. 35).

[59]   Kunyu Liang, Lok Shu Hui, and Ayse Turak. "Probing the multi-step crystallization dynamics of micelle templated nanoparticles: structural evolution of single crystalline γ-Fe$_2$O$_3$". In: *Nanoscale* 11.18 (2019-05), pp. 9076–9084. ISSN: 2040-3364. DOI: 10.1039/C9NR00148D. URL: http://xlink.rsc.org/?DOI=C9NR00148D (cit. on p. 42).

[60]   Matt Bumstead, Kunyu Liang, Gregory Hanta, Lok Shu Hui, and Ayse Turak. "disLocate: tools to rapidly quantify local intermolecular structure to assess two-dimensional order in self-assembled systems". In: *Scientific Reports* 8.1 (2018-12), p. 1554. ISSN: 2045-2322. DOI: 10.1038/s41598-017-18894-7. URL: http://www.nature.com/articles/s41598-017-18894-7 (cit. on pp. 44, 57).

[61]   R. B. Thompson, K. Rasmussen, and T. Lookman. "Origins of elastic properties in ordered block copolymer/nanoparticle composites". In: *Nano Letters* 4.12 (2004), pp. 2455–2459. ISSN: 15306984. DOI: 10.1021/nl048407f (cit. on pp. 47, 48).

[62]   Jiezhu Jin, Jianzhong Wu, and Amalie L. Frischknecht. "Modeling microscopic morphology and mechanical properties of block copolymer/nanoparticle composites". In: *Macromolecules* 42.19 (2009), pp. 7537–7544. ISSN: 00249297. DOI: 10.1021/ma9006686 (cit. on p. 47).

[63]   Dong Hyun Lee, Sung Hyun Han, Wonchul Joo, Jin Kon Kim, and June Huh. "Phase Behavior of Polystyrene- block -poly(4-vinylpyridine) Copolymers Coordinated by Metal Chloride". In: *Macromolecules* 41.7 (2008), pp. 2577–2583. ISSN: 0024-9297. DOI: 10.1021/ma702403k. URL: http://pubs.acs.org/doi/abs/10.1021/ma702403k (cit. on pp. 49, 52).

[64]   N H Agnew. "Transition Metal Complexes of Poly (viny1pyridines)". In: *Journal of Polymer Science* 14 (1976), pp. 2819–2830 (cit. on pp. 49, 52).

[65]   L. S. Hui, C. Beswick, A. Getachew, H. Heilbrunner, K. Liang, G. Hanta, R. Arbi, M. Munir, H. Dawood, N. Isik Goktas, R. Lapierre, M. C. Scharber, N. S. Sariciftci, and A. Turak. "Reverse Micelle Templating Route to Ordered Monodispersed Spherical Organo-Lead Halide Perovskite Nanoparticles for Light

Emission". In: *ACS Applied Nano Materials* 2 (2019), pp. 4121–4132. ISSN: 25740970. DOI: `10.1021/acsanm.9b00585` (cit. on pp. 58, 65).

[66] Maarten de Jong, Wei Chen, Thomas Angsten, Anubhav Jain, Randy Notestine, Anthony Gamst, Marcel Sluiter, Chaitanya Krishna Ande, Sybrand Van Der Zwaag, Jose J Plata, Cormac Toher, Stefano Curtarolo, Gerbrand Ceder, Kristin A Persson, and Mark Asta. "Charting the complete elastic properties of inorganic crystalline compounds". In: *Scientific Data* 2 (2015), pp. 1–13. DOI: `10.1038/sdata.2015.9` (cit. on p. 66).

[67] Xu Cao, Guoshun Pan, Peng Huang, Dan Guo, and Guoxin Xie. "Silica-Coated Core - Shell Structured Polystyrene Nanospheres and Their Size-Dependent Mechanical Properties". In: *Langmuir* 33 (2017). DOI: `10.1021/acs.langmuir.7b01777` (cit. on p. 68).

[68] Ailian Chen, Cheng Qian, Yang Chen, Xiaobing Zhao, and Naiming Miao. "Exploring the Elastic Behavior of Core–shell Organic–Inorganic Spherical Particles by AFM Indentation Experiments". In: *Journal of Inorganic and Organometallic Polymers and Materials* 24.6 (2014-11), pp. 1070–1076. ISSN: 1574-1443. DOI: `10.1007/s10904-014-0098-9`. URL: `http://link.springer.com/10.1007/s10904-014-0098-9` (cit. on p. 68).

[69] Siheng Sean You, Rossen Rashkov, Pongsakorn Kanjanaboos, Ignacio Calderon, Mati Meron, Heinrich M Jaeger, and Binhua Lin. "Comparison of the Mechanical Properties of Self-Assembled Langmuir Monolayers of Nanoparticles and Phospholipids". In: *Langmuir* 29 (2013). DOI: `10.1021/la4020064` (cit. on pp. 68, 70).

[70] Shilpa N Raja, Andrew C K Olson, Aditya Limaye, Kari Thorkelsson, Andrew Luong, and Liwei Lin. "Influence of three-dimensional nanoparticle branching on the Young ' s modulus of nanocomposites : Effect of interface orientation". In: *Proceedings of the National Academy of Sciences of the United States of America* 112.21 (2015), pp. 6533–6538. DOI: `10.1073/pnas.1421644112` (cit. on p. 77).